minerals

MDPI

Article

Barren and Li–Sn–Ta Mineralized Pegmatites from NW Spain (Central Galicia): A Comparative Study of Their Mineralogy, Geochemistry, and Wallrock Metasomatism

Ana Roza Llera, Mercedes Fuertes-Fuente *, Antonia Cepedal and Agustín Martin-Izard

Department of geology, University of Oviedo, Arias de Velasco s/n, 33005 Oviedo, Spain; rozaana@uniovi.es (A.R.L.); mcepedal@geol.uniovi.es (A.C.); amizard@geol.uniovi.es (A.M.-I.)

* Correspondence: mercedf@uniovi.es

Received: 31 October 2019; Accepted: 27 November 2019; Published: 29 November 2019

Abstract: In Central Galicia, there are occurrences of barren and Li–Sn–Ta-bearing pegmatites hosted by metasedimentary rocks. A number of common and contrasting features between Panceiros pegmatites (barren) and Li–Sn–Ta mineralized Presqueira pegmatite are established in this study. K-feldspar and muscovite have the same trace elements (Rb, Cs, P, Zn, and Ba), but the mineralized one has the highest Rb and Cs and the lowest P contents. The barren bodies show fluorapatite and eosphorite–childrenite replacing early silicates. The mineralized body has primary phosphates (fluorapatite and montebrasite), a metasomatic paragenesis (fluorapatite and goyazite) replacing early silicates, and a late hydrothermal assemblage (vivianite and messelite). Ta–Nb oxides from the Presqueira body show a trend from columbite-(Fe) to tantalite-(Fe) and tapiolite-(Fe). In this body, the Li-aluminosilicate textures support primary crystallization of petalite that was partially transformed into Spodumene + Quartz (SQI) during cooling, and into myrmekite during a Na-metasomatism stage. As a result of both processes, spodumene formed. The geochemical study supports magmatic differentiation increasing from the neighboring granites to the Li–Sn–Ta mineralized pegmatite. In both barren and mineralized bodies, the pegmatite-derived fluids that migrated into the wallrock were enriched in B, F, Li, Rb, and Cs and, moreover, in Sn, Zn, and As.

Keywords: wallrock signature; Li–Sn–Ta pegmatite; spodumene; petalite; myrmekite; columbite–tantalite; tantaliferous cassiterite; NW Spain

1. Introduction

Some rare elements, mainly those that support high-technology industry, have an increasing demand due to their variety of uses in new technologies. Among these elements, also known as high-technology metals, Ta, Li, and Sn are in high demand owing to their use in capacitors for wireless technology, in battery applications, and in liquid crystal displays (LCD) and touch-screen displays. These metals can occur in high concentrations in pegmatites and occasionally form ore deposits. Consequently, data to improve the prospecting criteria for rare metal ores in pegmatites are critical for the localization of undiscovered resources ([1] and references therein). The presence of Li–Sn–Ta mineralization associated with pegmatites is known in Galicia, northwestern Spain (e.g., [2–4]), and, moreover, there are several occurrences of barren pegmatites. This work focuses on a Li–Sn–Ta mineralized body, the Presqueira pegmatite, which is a non-outcropping body that has been recently explored by a mining company, and a swarm of pegmatites that are barren in Li–Sn–Ta bearing minerals, the Panceiros pegmatites. In this research, we have carried out a comparative study of the whole-rock and mineral geochemistry of the barren and the mineralized bodies and their host-rock together with

the possible parental granites. The main aim of this research is to evaluate tools for the exploration of Li–Sn–Ta enriched pegmatites such as trace-elements in major pegmatite-forming minerals and geochemical signatures of metasedimentary wall rock.

2. Geological Setting

The studied pegmatites are located in the vicinity of the village of Cerdedo (Pontevedra, Galicia), in NW Spain (Figure 1). Geologically, this area is in the Iberian Massif, which presents the westernmost exposures of the European Variscides in the southwestern limb of the arc described by this chain in Western Europe. The Iberian Massif has been divided into several zones [5], one of the innermost zones being the "Galicia Trás-Os-Montes Zone" (GTMZ), where these pegmatites are located. The GTMZ [6] represents a stack of allochthonous and parautochthonous units thrust over the autochthonous Central Iberian Zone (Figure 1). Two domains have been distinguished within the GTMZ ([6,7] and references therein): The Schistose Domain, also known as the Parautochthonous Domain, and the Allochthonous Complexes, emplaced over the parautochthonous pile and composed of ophiolitic and catazonal units of more exotic origin [8–10]. The studied pegmatites are in the Schistose Domain, which is an allochthonous sequence emplaced on the lower Paleozoic and Precambrian rocks of the Central Iberian Zone. This Domain is constituted by a lower Paleozoic metasedimentary sequence, more than 4000 m thick, interpreted as the most external sediments of the continental margin of Gondwana [6,7,10–14]. Two stratigraphic units, the lower one known as the Nogueira group and the upper one as the Paraño group, have been established in the Schistose Domain. The Paraño group (Figure 2), which hosts the Presqueira pegmatite, constitutes a more than 3000 m thick succession of siliciclastic rocks, Cambrian to lower Silurianin age [7]. In the studied area, this group is mainly formed by schist, some of them graphite-rich, and subordinate quartzite. In addition, some authors [6,15] define another stratigraphic unit underlying the Paraño Group, referred to as the Santa Baia group (Figure 2). Several authors (e.g., [13,16,17]) point out that the Santa Baia Group belongs to the Central Iberian footwall of the Schistose Domain. This stratigraphic group hosts the Panceiros pegmatites and is mainly made up of schist and paragneisses in the area of study.

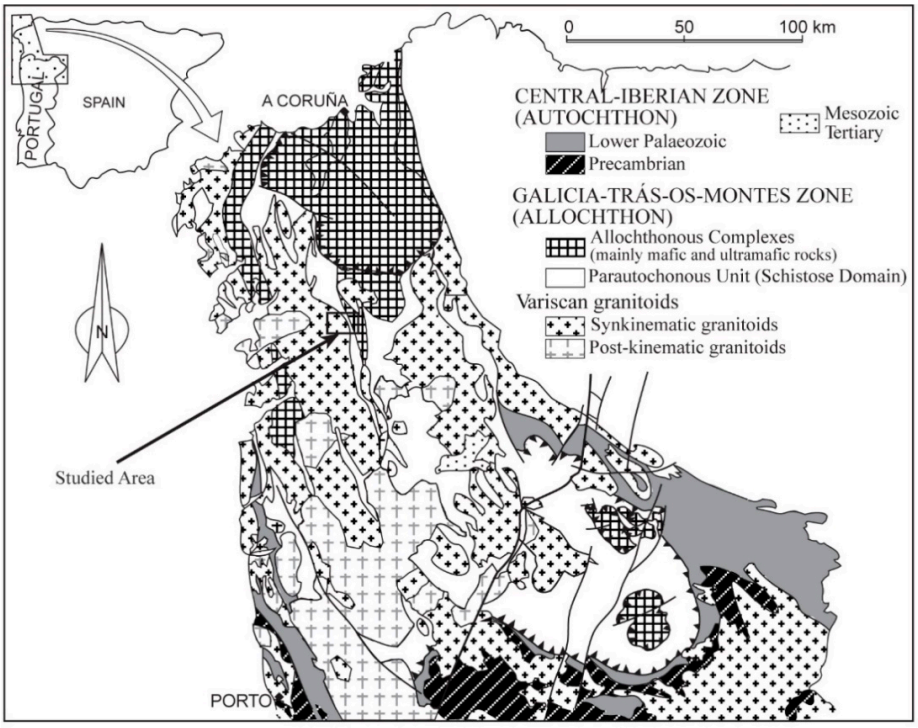

Figure 1. Geological map of the NW Iberian Massif showing the location of the studied area in the Galicia-Trás-Os-Montes Zone (modified from [9]).

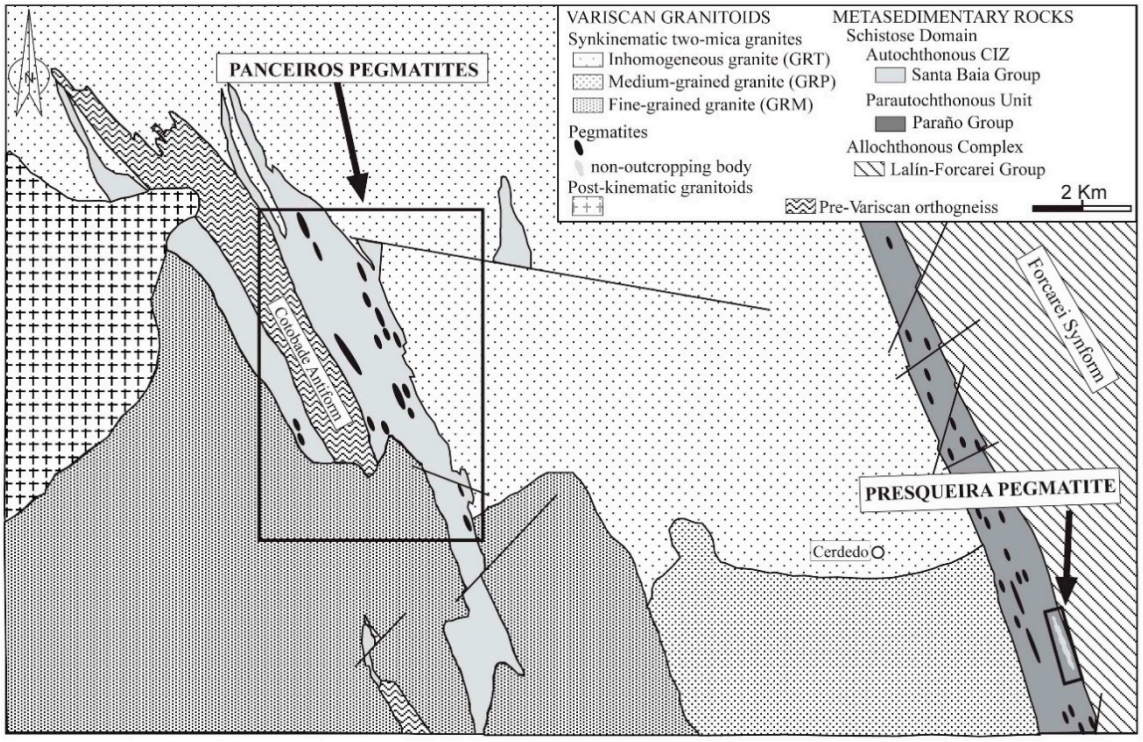

Figure 2. Schematic geological map showing the locations of the Panceiros pegmatites and the Presqueira pegmatite (adapted from [15]).

The tectonic style of the GTMZ is dominated by the thrust regime related to nappe emplacement during the Variscan Orogeny. There are two Variscan deformation events associated with nappe emplacement [7]: D1, recumbent folds with axial plane cleavage (S1), which are visible only when affecting the quartzite beds; and D2, also consisting of recumbent folds with axial plane crenulation cleavage or schistosity (S2) and having phyllonite fabrics developed in association with the Galicia- Trás-os-Montes basal thrust. After the nappe emplacement, the tectonic evolution becomes predominantly a wrench regime during the last deformation event (D3), which is characterized by folds with subvertical axial planes and shear zones (right folds) at all scales that include crenulation. At the same time, large volumes of synkinematic and late synkinematic granitoids are emplaced [11]. As regards the metamorphism, the Allochthonous Complexes have undergone an early high pressure (HP) metamorphism, which characterizes them but is not observed in the relative autochthon. The end of this HP metamorphism was dated at 374 Ma [18,19]. At the end of the emplacement of the allochthonous complexes to its present position, both allochthon and relative autochthon underwent a metamorphic event under greenschist-facies conditions [20]. Arenas [21] suggested that the temperature–pressure conditions of this episode were 375–425 °C and 2.5–3.5 kbar. The study of the deformation–recrystallization relationships during Variscan events shows that the peak of this metamorphism was reached during D2 [22]. Summarized data from the literature give ages for the main deformation events and metamorphism between 360–320 Ma [23], and the later deformation, which includes shear zones affecting the granites and the thermal aureoles [15], has been dated at about 315 ± 10 Ma [24].

In the area where the studied pegmatites outcrop, this medium-pressure metamorphism varies from the chlorite to sillimanite–orthoclase isograd [9] and is coeval with the development of a highly evolved schistosity (S2), which is affected by D3 crenulation [7]. During D3, NNW–SSE trending folds with vertical axial planes, such as the Cotobade Antiform and Forcarei Synform (Figure 2) fold of the previous structure, which is a major recumbent fold that verges eastwards. Moreover, during D3, a ductile shear zone affected the western limb of the Forcarei Synform [15]. According to

Barrera et al. [15], in the investigated area, synkinematic (D3) granitoids are widely exposed and have been subdivided into two suites on the basis of petrology and geochemistry [15]: (1) calc-alkaline biotite granites and (2) peraluminous two-mica or muscovite granites. The emplacement of the peraluminous granites produced a contact metamorphism that developed andalusite and biotite. In this area, these granites have not been dated. However, ages of similar synkinematic (D3) leucocratic granites have been obtained in the range of 330–310 Ma [24].

The Presqueira pegmatite is a non-outcropping body located in the northern end of the Forcarei Sur pegmatitic field (Figure 2). This field, defined by Fuertes-Fuente and Martin-Izard [2] and Fuertes-Fuente et al. [3], is located at the southern end of the Forcarei Synform western limb within the parautochthonous Paraño group. According to the above-mentioned authors, the Forcarei Sur pegmatitic field is made up of different types and subtypes of pegmatites belonging to the rare element class (beryl type, beryl–columbite–phosphate subtype, albite–spodumene type and albite type) with a cogenetic relationship and parental synkinematic (D3) leucocratic granite. The Panceiros pegmatites are located at the core of the Cotobade Antiform and within the probably autochthonous Santa Baia Group (Figure 2).

Most of the granites neighboring the studied pegmatites are synkinematic two-mica peraluminous granites. They were subdivided into several subtypes [15], on the basis of textural and mineralogical characteristics: (l) two-mica biotite-rich granite, (2) moderately leucocratic two-mica granite, (3) very leucocratic two-mica granite, and (4) inhomogeneous granite, which is a "mixture" of the other subtypes mentioned. The granites neighboring the pegmatites under study belong to two different subtypes, to the inhomogeneous granite, referred to in the text as GRT, and to two different facies of the moderately leucocratic two-mica granites. These facies are medium-grained granite, denoted GRP in the text, and fine-grained granite, referred to in the text as GRM (Figure 2). All of these granites produced contact aureoles containing andalusite and biotite.

3. Analytical Techniques

Pegmatite bodies from Panceiros and the Presqueira pegmatite were sampled. In the latter, the samples were taken from exploration adits. Representative samples from the neighboring granites and pegmatite host-rocks were also collected. The sample suite was chosen for mineralogical and petrographic studies and for the lithogeochemical study. The samples were studied by transmitted- and/or reflected-light microscopy, SEM-EDS (JEOL-6610LV), and EPM (CamecaSX100) at Oviedo University (Spain). Regarding analytical conditions for electron-microprobe analyses of phosphates and silicates, major elements were determined at 15 kV accelerating potential and 15 nA beam current, and an acquisition time between 5 and 20 s for X-ray peak and background, except for Sn, which was 80 s. In order to attain lower limits of detection (LOD), for some trace elements (i.e., Zn, Ga, Rb, Cs, Sr, and Ba), the operating conditions were 20 kV, 100 nA, and 30–60 s counting time. The LOD were 233 ppm for Sn, 90 ppm for Zn, 168 ppm for Ga, 99 ppm for Rb, 1289 ppm for Cs, 519 ppm for Sr, and 111 ppm for Ba (95% confidence). In oxides, elements were determined at 20 kV, 40 nA, and an acquisition time of between 10 and 20s. The LOD for In was around 900 ppm. In addition, sphalerite was also analyzed in order to check the presence of In and Ga, the LOD were 133 ppm and 113 ppm, respectively. The standards were albite (Na), jade (Si), MgO (Mg), orthoclase (K), vanadinite (Cl), andradite (Ca), MnTi (Mn, Ti), magnetite (Fe), apatite (P,F), SnO_2 (Sn), ZnS (Zn), AsGa (Ga), IR-X (Rb), celestite (Sr), CsIn (Cs), CELS (Ba), $MnWO_4$ (W), Nb_2O_5(Nb), pyrite (S), Cd (Cd), PbS (Pb), In (In), Ta (Ta), U-bearing glass (U), and Th-bearing glass (Th). In all electron-microprobe analyses, the standard deviation of results is less than 0.1%. The acquired X-ray intensities were corrected for atomic number, mass absorption, and secondary fluorescence effects using the CAMECA x-phi program.

For the lithogeochemical study, sample preparations were carried out at the Geology Department of Oviedo University. Rock samples from 0.5 kg to approximately 3 kg, in the case of pegmatites, were crushed, sieved, and finally, pulverized to at least 150 mesh. The whole-rock analyses were performed

in AcmeLabs commercial laboratories. Major and trace element concentrations were obtained using 4-acid digestion by ICP-emission spectrometry and by ICP mass spectrometry, respectively.

4. The Panceiros Pegmatites

Several pegmatites hosted by mica schist of the Santa Baia Group outcrop in the vicinity of Panceiros village. These bodies mainly occur in the eastern limb of the Cotobade Antiform and are aligned parallel to the boundaries of the mica schist band (Figure 2). The bodies have an N175E strike, coincident with the regional schistosity (S2), and subvertical dip. They emplaced during D3, when the Cotobade Antiform formed, and coeval with the regional emplacement of the synkinematic (D3) leucocratic granites. The dimensions of these bodies are variable, ranging from 2 to 30 m in length and from less than 1 m up to 10 m in width. The smaller bodies have an ellipsoidal shape and an internal structure characterized by a fine-grained groundmass with randomly distributed aggregates of K-feldspar as euhedral crystals of up to 60 cm. The larger bodies are tabular-shaped pegmatite with a layered internal structure characterized by coarse-grained bands dominated by K-feldspar and by thicker fine-grained bands. The contact between the pegmatites and the host rock is usually clearly defined, although there are more irregular contacts showing xenoliths of the host schist embedded by the pegmatite. Tourmalinization of the host rock at the contact with these igneous bodies is observed.

Mineralogy and Geochemistry

The main minerals in the Panceiros pegmatites are albite, perthitic K-feldspar, quartz, and muscovite. Albite ($Ab_{98.8}$–$Ab_{99.7}$) is dominant in the fine-grained (aplitic) bands, whereas K-feldspar dominates in the coarse-grained bands. Albite crystals sometimes contain irregular-shaped K-feldspar islands frequently associated with abundant fine-grained muscovite. Under cross-polarized light, the K-feldspar islands in a single albite grain are optically continuous and extinguish in the same direction (Figure 3a). This texture supports the replacement of K-feldspar by the plagioclase [25]. The accessory minerals are almandine ($Alm_{54–67}$, $Sps_{32–44}$, $Prp_{0.2–0.9}$, $Adr_{0.2–0.4}$), very scarce biotite, and phosphates.

Results from electron-microprobe analyses done in K-feldspar and albite can be found in Tables A1 and A2, respectively. K-feldspar has Rb and P as the main trace elements. Rubidium contents vary between 2700 and 3300 ppm. Phosphorus concentrations are quite homogenous among crystals from 2200 to 2500 ppm. Cesium sometimes occurs and attains contents above the limit of detection (LOD = 1289 ppm) of around 1700 ppm. Another trace-element is Zn, ranging from below from LOD (90 ppm) to 150 ppm, and, more rarely, some K-feldspar crystals have Ba contents of around 120 ppm. As regards albite, the main trace elements are Rb, showing consistent contents of around 2200 ppm among crystals and P. The latter varies widely among crystals from 550 ppm up to 3505 ppm. Barium, in much lower concentrations (140 ± 20 ppm), is seldom detected.

Electron-microprobe analyses in muscovite, according to the Monier and Robert [26] classification (Figure 4), show F contents between 0.2 and 0.5 wt % (Table A3). The trace elements determined were Rb, Cs, P, and Zn. Rubidium has homogenous contents from 2100 to 3300 ppm, whereas Cs, as in K-feldspar, varies from undetected (or below LOD) up to 2200 ppm. Measurements of P and Zn always reveal contents of between 212 and 430 ppm, and from 280 to 370 ppm, respectively.

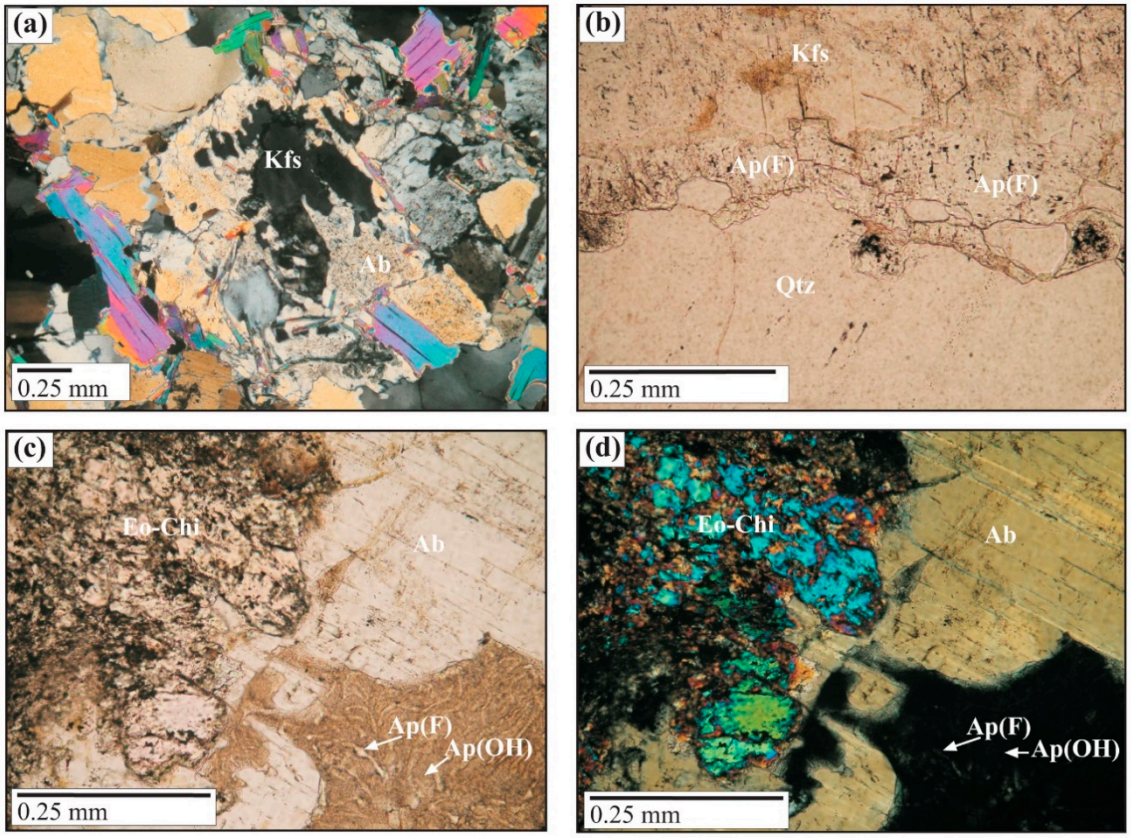

Figure 3. Photomicrographs of samples from the barren pegmatites of Panceiros: (**a**) irregular relicts of K-feldspar (Kfs) in an albite (Ab) crystal under cross-polarized light. Note that the K-feldspar relicts are optically continuous; (**b**) crystal aggregate of Mn-rich fluorapatite, Ap(F), infilling a interstice between quartz (Qtz) and K-feldspar (Kfs); (**c**) albite (Ab) with irregular patches of eosphorite–childrenite (Eo–Chi) and argillized hydroxylapatite, Ap(OH), with fluorapatite Ap(F) relicts, under plane-polarized light; (**d**) the same mineral assemblage under cross-polarized light.

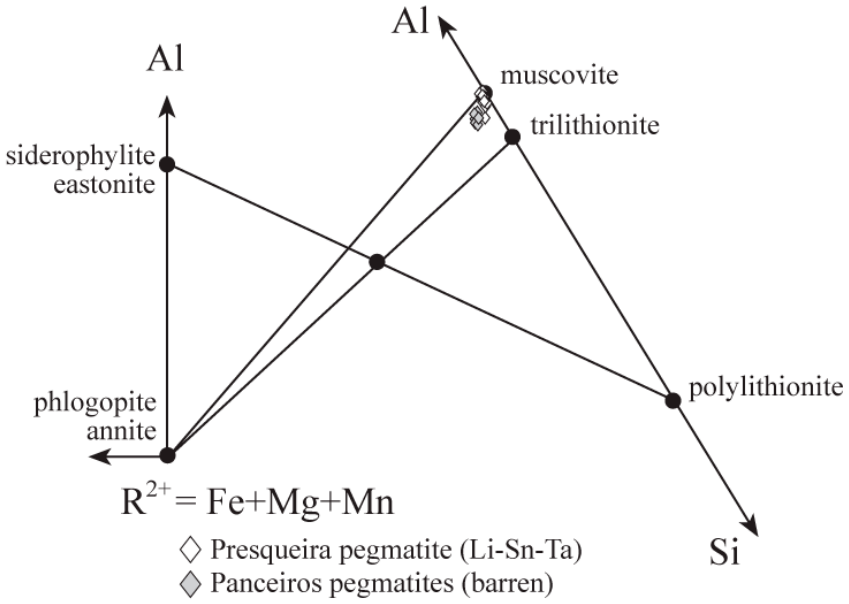

Figure 4. Chemical composition of white mica from the Panceiros and the Presqueira pegmatites plotted on the triangular diagram as a function of Al (IV + VI)–R^{2+}–Si (apfu), according to [25].

Chemical composition of garnet from Panceiros pegmatites (Table A4) vary in the almandine–spessartine solid solution with Mn/(Mn + Fe) ratios between 0.31 and 0.42. The most remarkable feature is the consistent presence of P contents ranging from 0.2 to 0.3 wt % P_2O_5. Haggerty et al. [27] and Burt [28] suggested these three possible substitutions in garnet: $AlP Si_{-2}$, $MnP(AlSi)_{-1}$, and $NaP(R^{2+}Si)_{-1}$, other potential substitutions have also been proposed by Breiter et al. [29]. The substitution involving sodium is not applicable to the studied garnets due to a lack of this element in the studied samples. Figure 5 unambiguously shows that P enters the garnet of the Panceiros pegmatites by means of the substitution mechanism of $AlP Si_{-2}$. Other authors [30–32] also propose this substitution in garnets from granitic pegmatites.

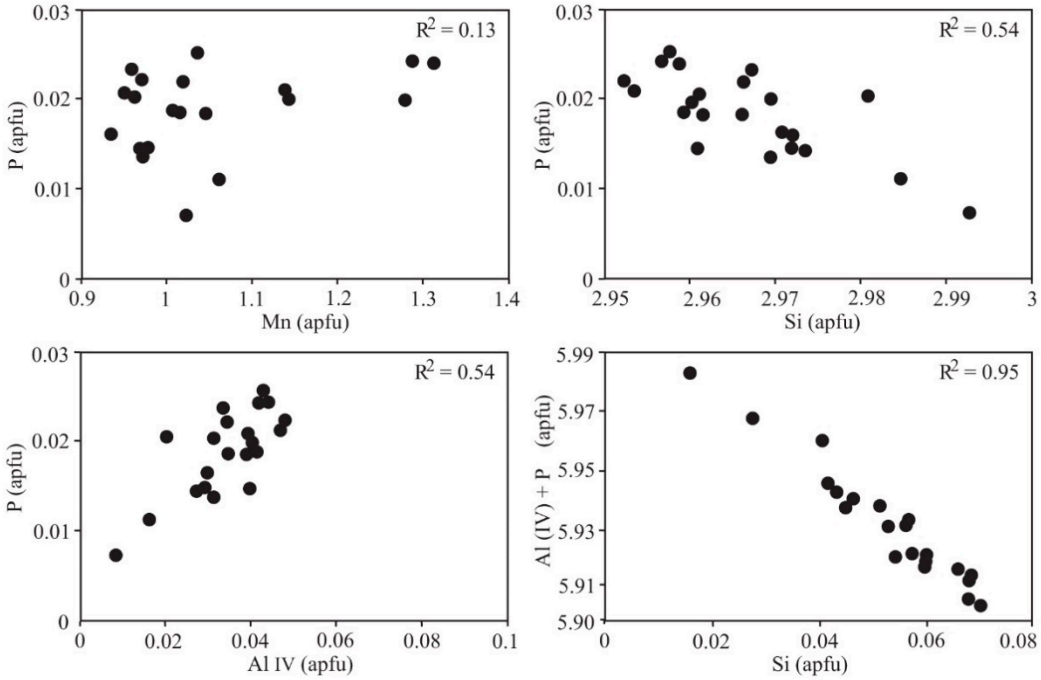

Figure 5. Plots (in apfu) of Mn vs. P, Si vs. P, Al (IV) vs. P, and Si vs. Al (IV) + P for garnet from the Panceiros pegmatites.

The identified phosphates belong to the apatite group and to the eosphorite–childrenite series (Table A5). Despite the lack of X-ray diffraction data, transmission optical microscopy properties, scanning electron microscopy coupled with energy dispersive X-ray spectroscopy (SEM-EDS) data together with electron-microprobe analyses allowed us to identify the phosphates described in this work. According to optical microscopy and backscattered-electron images from SEM-EDS, apatite shows different textures that match different compositions. This mineral appears isolated as colorless subeuhedral crystals or forming irregular crystal aggregates infilling interstices between the main silicates (Figure 3b). From EPM analyses (Table A5), it can be classified as Mn-rich fluorapatite, using Pasero et al. [33] nomenclature, with up to 5 wt % of MnO. This fluorapatite is partially replaced by brownish masses of a second generation of apatite, which is pervasively argillized (Figure 3c,d). This alteration prevents us from obtaining pristine analyses (Table A5); nevertheless, this apatite has much lower contents in F and Mn, being probably hydroxylapatite. It also occurs as patches replacing feldspars and more scarcely in open cavities and veinlets. Aluminum phosphates with compositions varying from eosphorite to an intermediate member of the eosphorite–childrenite series (Table A5) form similar irregular patches corroding albite and K-feldspar crystals. In fact, it is common to observe a feldspar crystal in which both the aluminum phosphate and the altered hydroxylapatite with fluorapatite relicts form replacement patches (Figure 3c,d). The argillized hydroxylapatite represents an alteration product of previously formed fluorapatite.

5. The Presqueira Pegmatite

The Presqueira pegmatite is a non-outcropping tabular body with a main dike that forks into several branches and reaches 700 m in length and up to 15 m in width, according to NI 43-101 Technical Report of resource estimate [34]. The pegmatite is hosted by quartz-schists of the Paraño Group and strikes N160E, being concordant with the regional schistosity (S2). The body is subhorizontal at the northern end and dips 40° towards the west at the southern end.

In the exploration adits, it is possible to observe the clearly defined contact between the pegmatite and the host schist, which shows tourmalinization. The body can be referred to as pegmatite-aplite since it has a layered internal structure with coarse-grained (pegmatitic) bands and fine-grained (aplitic) bands. This magmatic layering, which runs approximately parallel to the host-rock contact, is continuous at the macro-and microscopic scale in both aplite and pegmatite bands. However, a mylonitic texture, more noticeable in the pegmatitic bands, is superimposed on the magmatic layering. This tectonic fabric may be associated with the shear zone developed in this area during the third tectonic phase (D3) of the Variscan orogeny.

Mineralogy and Geochemistry

The Presqueira pegmatite is mainly composed of plagioclase ($Ab_{99.6}$–Ab_{100}), spodumene, quartz, muscovite, and perthitic K-feldspar found chiefly in pegmatitic bands. The accessory minerals are petalite, which mainly occurs associated with K-feldspar in the pegmatitic bands, Sn–Ta–Nb bearing oxides, more abundant in the aplitic bands, and phosphates. Uraninite, sphalerite, and arsenopyrite occur in much lower proportions.

Albite frequently shows myrmekites, and some crystals have a turbid core that is mantled by a clear myrmekite rim (Figure 6a). This core sometimes has K-feldspar relicts similar to those described for Panceiros pegmatites (Figure 6a). The abundance of textures indicative of the albitization of K-feldspar is a striking petrographic characteristic of the Presqueira pegmatite.

Electron-microprobe analyses of K-feldspar (Table A1) indicate that the more abundant trace elements are Cs, Rb, and, in lower concentrations, P. Rubidium contents are between 4700 and 5800 ppm. Cesium concentrations range from 3200 to 6400 ppm. Phosphorus concentrations vary from 1800 to 3000 ppm. Zinc has contents of around 150 ± 40 ppm, and Ba is seldom detected. In albite (Table A2), the main trace elements are Rb and P. The former shows consistent contents of around 2200 ppm among crystals, in contrast to the latter that shows highly variable concentrations from 195 up to nearly 3000 ppm. In much lower proportions, Ba is also detected above the LOD and varies from 140 to 240 ppm.

Regarding muscovite (Figure 4), EPM analyses (Table A3) show F contents of between 0.13 and 0.33 wt %. The main trace elements are Rb, Cs, and, in lower concentration, Zn. Rubidium has homogenous contents from 3600 ppm to 4800 ppm, whereas those of Cs are more variable, from 2000 up to 4800 ppm, the more frequent interval lying between 3500 and 4500. Zinc is always detected with contents of between 174 ppm and 368 ppm. Barium is sometimes detected with contents ranging from 116 to 170 ppm.

The most abundant lithium aluminosilicate is spodumene, which occurs in the following two different forms. It appears as coarse-grained spodumene–quartz intergrowths (Figure 6b). These resemble the spodumene–quartz intergrowth known as SQI resulting from the pseudomorphic replacement of petalite defined by Černý and Ferguson [35]. In fact, in some samples, it is possible to observe this intergrowth replacing petalite (Figure 6b). The spodumene also occurs as aggregates of subeuhedral crystals in the interface between feldspar grains. In this case, the lithium aluminosilicate often develops a narrow rim consisting of a fine-grained vermicular quartz–spodumene symplectitic intergrowth (Figure 6c). This texture has also been described in other pegmatites in this pegmatitic field [36] and also in the bodies of the Kangxiwa–Dahongliutan pegmatite field in the Western Kunlun Orogen of China [37].

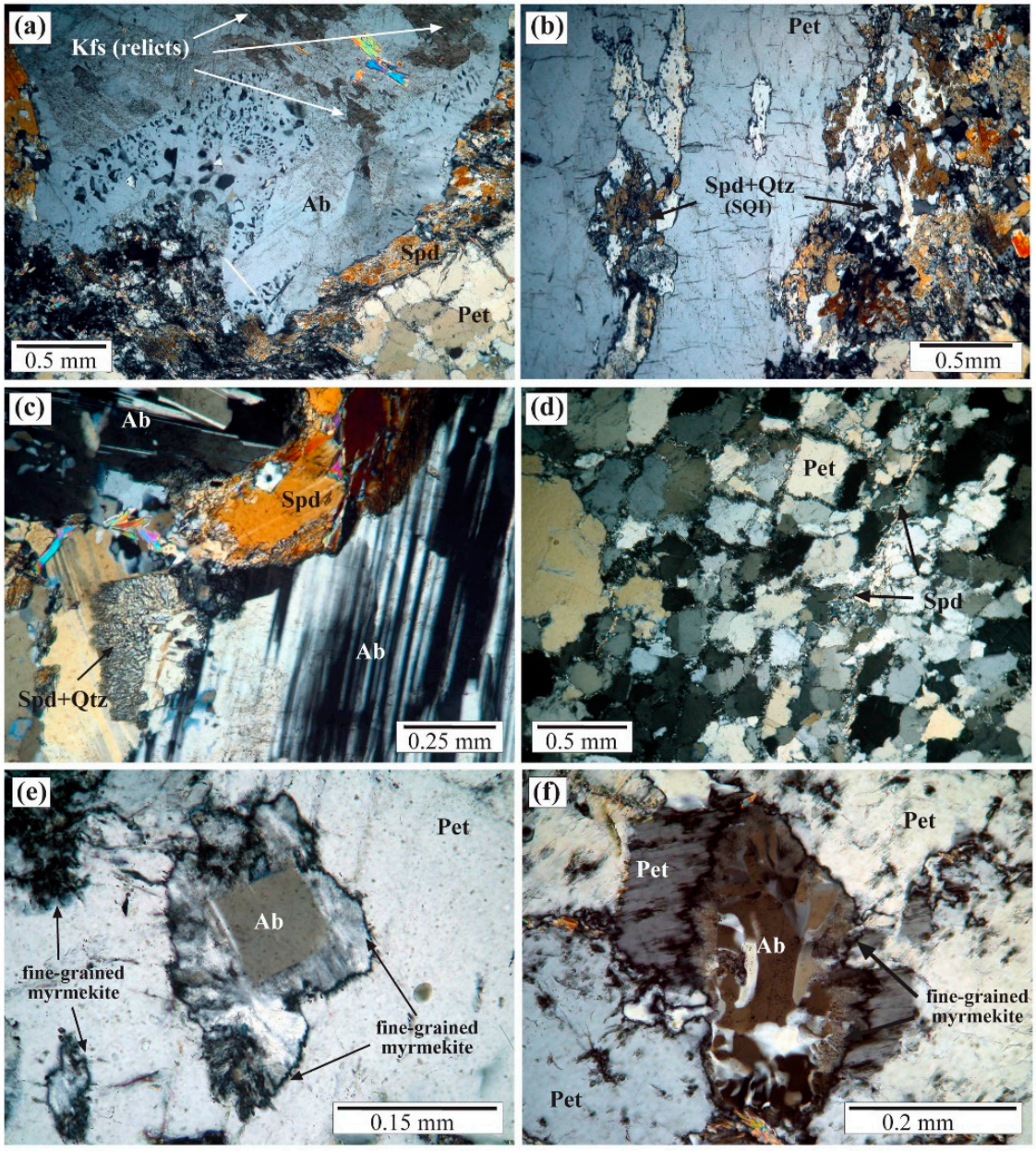

Figure 6. Photomicrographs of samples from the Li–Sn–Ta ore-bearing pegmatite of Presqueira: (**a**) albite crystal with a turbid core showing K-feldspar relicts. The core is mantled by a clear myrmekite rim. Note the presence of spodumene between the albite crystal and the petalite aggregates; (**b**) spodumene+quartz replacement (SQI) of petalite; (**c**) spodumene crystals with a fine-grained symplectitic quartz–spodumene intergrowth at the contact with neoformed albite. Note that from the contact rim between both minerals towards the inner parts of the spodumene crystal, the symplectitic intergrowth shows grain coarsening. Note the myrmekites (upper left corner of the image); (**d**) aggregate of petalite crystals with tiny acicular spodumene replacing them along crystal boundaries; (**e**) Petalite partially replaced by irregular patches of extremely fine-grained myrmekites. In the image center, one of this patch shows neoformed albite in the core; (**f**) Petalite replaced by mymekite. Note a rim that coarsens away from the contact with petalite resulting in albite showing coarse-grained myrmekites. Quartz (Qtz), petalite (Pet), spodumene (Spd), albite (Ab) and K-feldspar (Kfs). See text for further explanation.

Petalite occurs as aggregates of euhedral crystals (Figure 6d) or as coarser-grained isolated crystals (Figure 6b). As previously mentioned, some petalite crystals are replaced by the above-mentioned SQI.

In some samples, petalite aggregates are replaced by tiny acicular spodumene along crystal boundaries (Figure 6d). In addition, petalite is replaced by extremely fine-grained myrmekites that coarsen away from the contact, with petalite transformed into albite with a fine-grained myrmekite rim (Figure 6e) or, more frequently, albite showing coarse-grained myrmekites (Figure 6f). The latter resembles the common form of albite occurrence in this pegmatite.

As regards phosphates, Mn-bearing fluorapatite is the most abundant one in this pegmatite (Table A6). It often appears as isolated colorless euhedral crystals. Occasionally, it forms intergrowth with silicates or other phosphates. In addition, two different aluminous phosphates have been identified. The more common Al-rich phosphate in this pegmatite is montebrasite with F/(F + OH) < 0.30 (Table A6). It is commonly associated with spodumene and forms isolated euhedral–subeuhedral crystals. The other identified aluminum phosphate belongs to the crandallite series, goyazite being the Sr-rich member (Table A6). It forms irregular acicular crystal aggregates that are occasionally intergrown with fluorapatite. These aggregates fill open spaces or replace K-feldspar (Figure 7a,b).

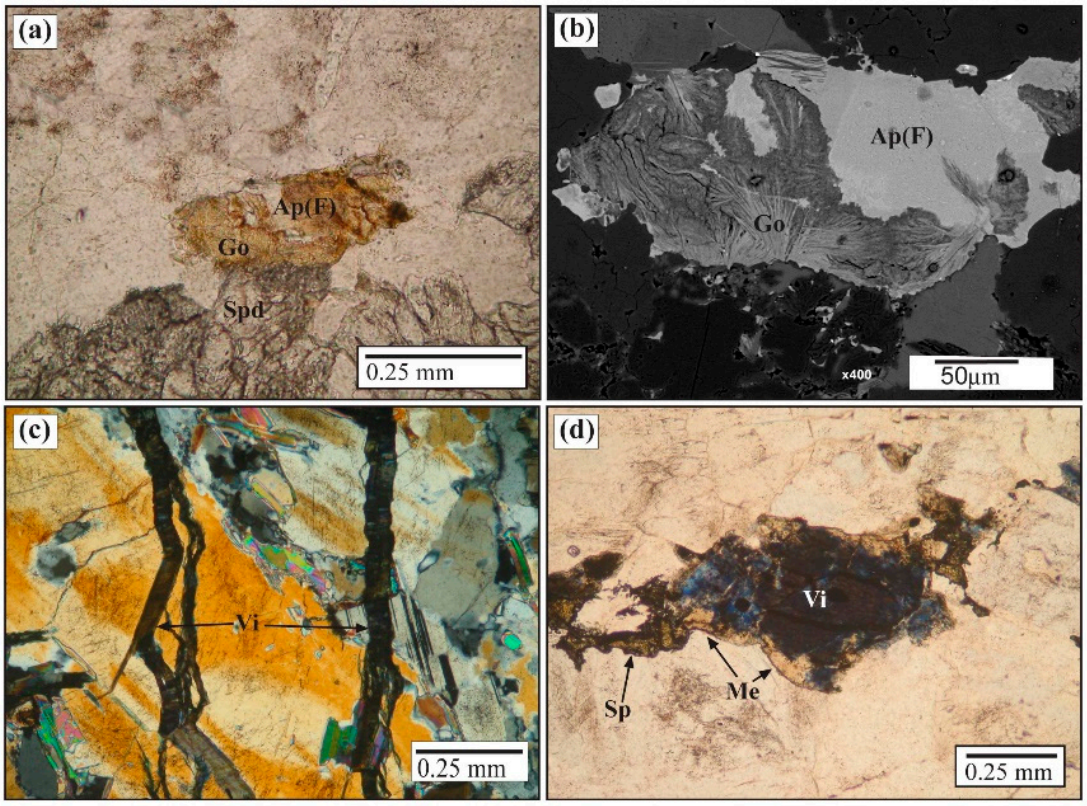

Figure 7. Photomicrographs of samples from the Li–Sn–Ta ore-bearing pegmatite of Presqueira; (**a**) goyazite (Go) and fluorapatite, Ap(F), filling an open space, under plain-polarized light; (**b**) backscattered electron (BSE) image of the mineral assemblage of Figure 7a enlarged. Note that goyazite forms acicular crystal aggregates and is intergrown with fluorapatite; (**c**) vivianite (Vi)-bearing veinlets crosscutting an albite-rich band, under cross-polarized light; (**d**) irregular veinlet filled with vivianite (Vi) partially replaced by messelite (Me) together with sphalerite (Sp), under plain-polarized light.

Finally, the Fe–Mn–Ca phosphates vivianite and messelite (Table A6) were identified, filling cavities and late veinlets that crosscut the whole body (Figure 7c). These veinlets are very abundant and an outstanding characteristic in hand samples due to the deep blue color of the vivianite. Vivianite is sporadically associated with messelite. In such cases, vivianite is partially replaced by messelite accompanied by sphalerite (Figure 7d).

The Sn–Ta–Nb bearing oxides are cassiterite and members of the columbite–tantalite group. These minerals commonly occur disseminated in the fine-grained aplitic bands of the Presqueira body. Cassiterite often appears as twinned subeuhedral crystals. This oxide is mainly enriched in Ta and Nb (Ta + Nb up to 4.5 wt %) with Ta/(Ta + Nb) = 0.5–1.0, having lower contents of Fe (1000–7500 ppm), In (1000–1500 ppm), and Ti (600–1200 ppm) (Table A7). Under transmitted light optical microscopy, this oxide commonly reveals color zoning with dark reddish-brown and clear yellow growth bands of variable thickness. The dark bands are the richest in Ta and Nb together with the above-mentioned trace elements. Moreover, cassiterite sometimes presents columbite–tantalite inclusions or is intergrown with this mineral.

Columbite–tantalite often forms fine-grained euhedral to subeuhedral crystals with prismatic and tabular habits. Uraninite, which sometimes has thorium contents of up to 5000 ppm, is occasionally present as inclusions or as intergrowths at the border of the columbite–tantalite crystals (Figure 8a,b). SEM backscattered images of discrete columbite–tantalite grains show euhedral cores mainly enriched in Nb and rims of variable thickness enriched in Ta (Figure 8c–e). Cores and rims usually present fine oscillatory zoning (Figure 8) that sometimes exhibits truncated layers, mainly in the Nb-richer core (Figure 8e). In addition, the rims are sometimes irregular, resulting in a sub-euhedral to anhedral crystal with a euhedral prismatic core (Figure 8f). On other occasions, the contact of these Ta-rich rims with the Nb-rich cores is lobate, giving rounded corners, and embayments (Figure 8a,b,f). In some crystals, the oscillatory zonation of Nb-rich cores is partially disrupted by a patchy Ta-richer zonation (Figure 9a), to use the Lahti [38] nomenclature. Discontinuities in growth marked by corrosion and patchy zoning suggest replacement processes [39]. Superimposed upon the described zonation patterns, anhedral tapiolite-(Fe) (Table A7 and Figure 9) occurs at the margins of the grains or along microfractures, which leads us to interpret it as evidence of this phase representing the last Ta–Nb oxide formed in the paragenesis. The composition of cores corresponds to columbite-(Fe) with Ta/(Ta + Nb) = 0.10−0.47 and Mn/(Mn + Fe) = 0.35−0.52 (Table A7 and Figure 10). Rim composition varies between columbite-(Fe) and tantalite-(Fe) with Ta/(Ta + Nb) = 0.37−0.65 and Mn/(Mn + Fe) = 0.20−0.49 (Table A7 and Figure 10). The Ta/(Ta + Nb) and Mn/(Mn + Fe) ratios of the individual crystals (Figure 10) exhibit significant changes and follow two main evolutionary trends. A trend characterized by an increase in the Ta ratio (Ta/Ta + Nb) at near-constant Mn ratio (Mn/Mn + Fe) (Figure 8b,c,e and Figure 10), and a trend characterized by increasing Ta ratio at decreasing Mn ratio (Figure 9a,b and Figure 10).

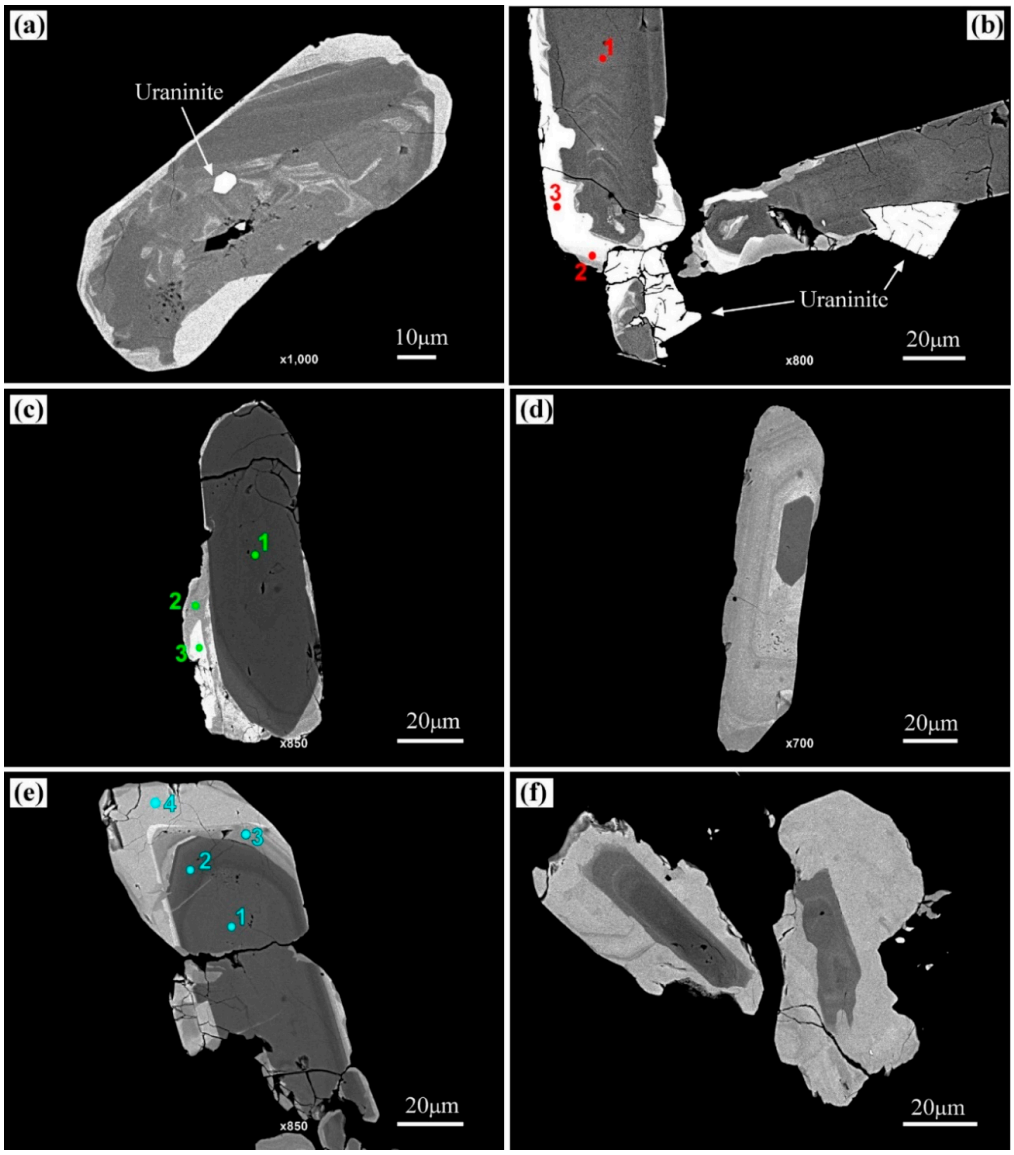

Figure 8. SEM-BSE images of columbite–tantalite crystals from the Presqueira pegmatite. In these images, the darker the grey color is, the richer is the composition in Nb. Numbers and dots (red, green, and blue) correspond to the zone of the crystal plotted in the compositional columbite–tantalite quadrilateral of Figure 10; (**a**) euhedral prismatic crystal of columbite–tantalite with an inclusion of a tiny uraninite crystal. The columbite–tantalite grain shows a discontinuous oscillatory-zoned core, with mainly columbite-(Fe) composition partially corroded by Nb-poorer patch with complex zoning, surrounded by an irregular thinner rim with embayments of tantalite-(Fe) composition; (**b**) columbite–tantalite grains with tiny uraninite crystals attached at their borders. Note the left-hand crystal showing a fine-oscillatory zoned core, columbite-(Fe), a Nb-poorer irregular rim with complex zoning, and a lobulated rim of tantalite-(Fe) composition; (**c**) a prismatic columbite–tantalite crystal with oscillatory zoning in the core, columbite-(Fe), a Nb-poorer irregular rim with complex zoning, and a narrow rim of mostly tantalite-(Fe) composition; (**d**) a prismatic columbite–tantalite crystal showing a small homogenous core of columbite-(Fe) and a thicker fine-oscillatory zoned rim of chiefly tantalite-(Fe) composition; (**e**) euhedral oscillatory zoned columbite–tantalite grain exhibiting truncated layers suggesting episodes of partial dissolution and successive crystallization; (**f**) sub-euhedral columbite–tantalite grains showing fine-oscillatory zoned cores, mostly columbite-(Fe), and thick fine-oscillatory zoned rims of mainly tantalite-(Fe). In the right-hand crystal, note the core containing inward-penetrating embayments of the rim. In the right-hand of the image, the bright tiny crystals are uraninite.

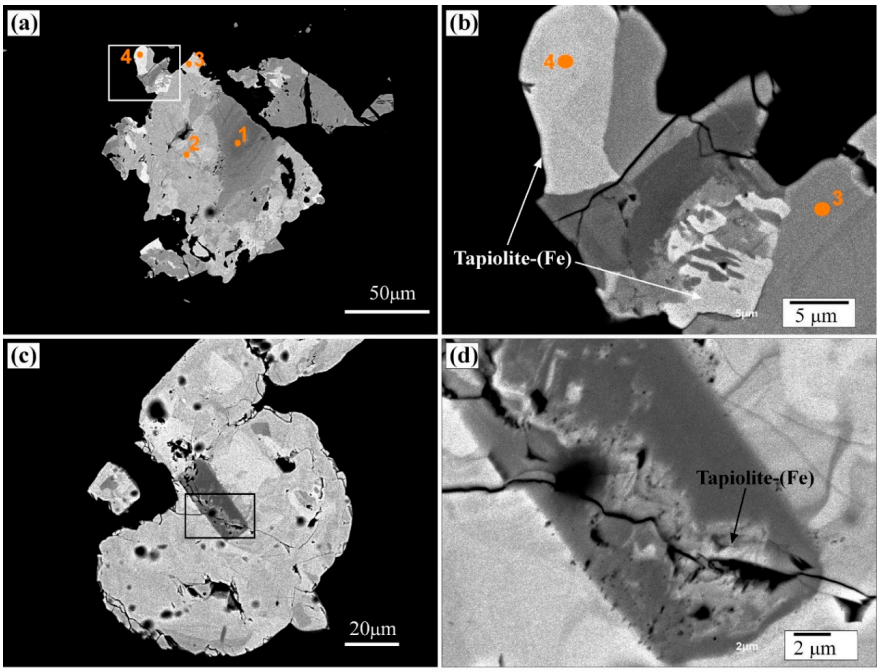

Figure 9. SEM-BSE images of columbite–tantalite crystals from the Presqueira pegmatite. Orange numbers and dots correspond to the zone of the crystal plotted in the compositional columbite–tantalite quadrilateral of Figure 10; (**a**) anhedral grain of columbite–tantalite showing Nb-richer oscillatory zoning partially disrupted by Ta-richer patchy zoning; (**b**) tapiolite-(Fe) at the margins of a columbite–tantalite grain, enlarged field corresponding to the white rectangle of Figure 9a; (**c**) sub-euhedral sillimanite grain showing a core, mostly columbite-(Fe) and a very thick Ta-richer rim; (**d**) tapiolite-(Fe) filling a microveinlet that crosscuts a columbite–tantalite grain, enlarged field corresponding to the black rectangle of Figure 9c.

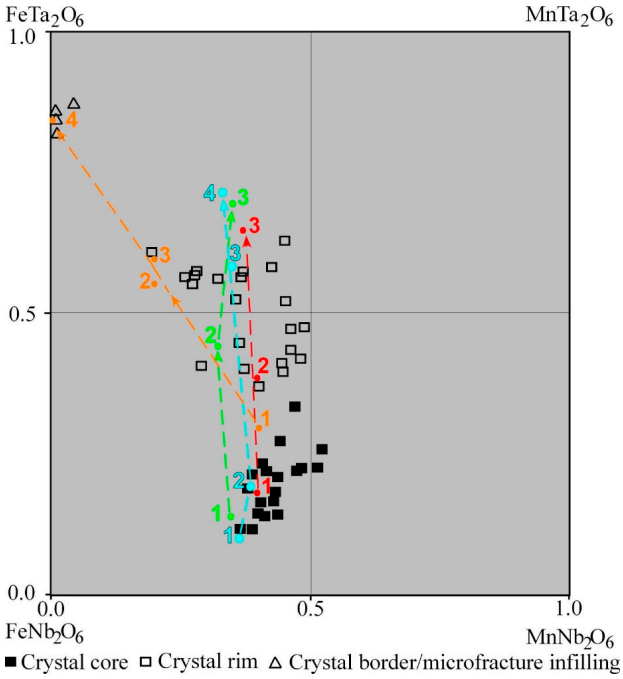

Figure 10. Compositions of Ta–Nb oxides from the Presqueira pegmatite plotted in the columbite–tantalite quadrilateral, Mn/(Mn + Fe) vs. Ta/(Ta + Nb). The compositional variations of the individual crystals of Figure 8b,c,e, and Figure 9a,b are also plotted (numbers and dots correspond to those of the crystals from these figures).

6. Whole Rock Geochemistry

For whole-rock geochemical analyses, pegmatite outcrops of five bodies were sampled in the Panceiros area. In the sampling, an effort was made to take representative samples of both aplitic and pegmatitic bands for each body. In the Presqueira pegmatite, four samples were taken from the footwall to the hanging wall in an exploration adit that traversed the body. Furthermore, representative samples of the main granites outcropping in the area, i.e., GRP, GRM, GRT (Figure 2), were taken.

6.1. Igneous Rock Geochemistry: Pegmatites and Granites

All samples from the Panceiros bodies and the Presqueira pegmatite (Figure 11, Table A8) are characterized by similarly high contents in SiO_2, higher than 73 wt %, and low in CaO and Fe_2O_3 (<1 wt %), although the latter clearly shows the lowest concentration in the Presqueira body. MgO, MnO, and TiO_2 contents are low and also similar among the pegmatites bodies (<0.1 wt %). The Na_2O/K_2O ratio is comparable in the Panceiros bodies from 0.9 to 1.5 (mode close to 1) but lower than that of the Presqueira pegmatite, which reaches a maximum of two. All of them have very similar ASI and A/CNK indexes due to their low Ca contents. ASI and A/CNK values are comparable among Panceiros bodies, ranging from 1.26 to 1.36 and from 1.18 to 1.32, respectively, whereas the Presqueira body reveals higher values of 1.54 and 1.49, respectively. According to these indices, the studied pegmatites are peraluminous, but the Presqueira pegmatite has a stronger peraluminous character. Phosphorus concentrations are quite similar in all the studied bodies, varying between 0.2 and 0.6 wt % P_2O_5. Regarding the sampled granites (Figure 11), they have high silica contents (72–73 wt % SiO_2) (Table A8). The Fe_2O_3, CaO, MgO, TiO_2, and MnO are low but higher than those of the pegmatites. They are peraluminous, their ASI and A/CNK indexes lying between 1.35 and 1.40, and from 1.23 to 1.31, respectively. They contain relatively high total alkali concentrations, with K_2O concentrations of 4.81–5.33 wt %, Na_2O concentrations of 3.03–3.26 wt %, and total K_2O + Na_2O ranging from 8.07 to 8.46 wt %. In contrast to the pegmatites, the granites have a clearly higher K than Na content, the Na_2O/K_2O ratio being (0.6) lower than that of the pegmatites. Phosphorus concentrations are between 0.23 and 0.35 wt % P_2O_5.

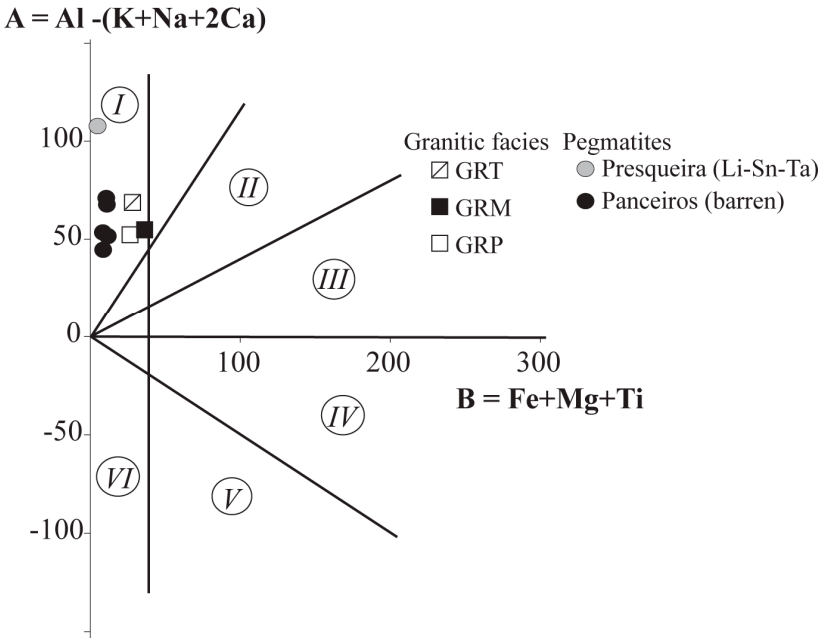

Figure 11. Plot of the whole-rock compositions from the studied pegmatites and the granites neighboring the pegmatites in the A–B diagram of Debon and Le Ford [40]. Granitic facies: GRP moderately leucocratic, medium-grained two-mica granite, GRM moderately leucocratic, fine-grained two-mica granite, and GRT inhomogeneous granite. I, II, III = peraluminous series; IV, V, VI = metaluminous series.

With regard to the analyzed trace elements (Table A8), the Presqueira pegmatite has strikingly higher contents than those of the Panceiros bodies in elements such as Li (>2000 ppm), Be (145 ppm), Rb (999 ppm), Cs (59 ppm), Nb (66 ppm), Ta (64 ppm), Sn (845 ppm), Sr (94 ppm), and Zn (99 ppm). The high contents in elements such as Li, Sn, Ta, Nb, Sr, and Zn are supported by the previously described mineralogy, i.e., spodumene, montebrasite, petalite, cassiterite, columbite–tantalite, goyazite, and Zn-bearing muscovite together with sphalerite. On the other hand, the Panceiros bodies have higher contents in Ba, Y, and, remarkably, in As. In fact, one of the sampled pegmatites reaches 593 ppm As despite the fact that As-bearing phases, such as arsenopyrite, have not been recognized in any of the studied samples. As regards the trace element amounts in the granites of the area, they have lower concentrations than pegmatites in some incompatible elements such as Be, Rb, Nb, Ta, and Sn (Table A8). However, Cs concentration in granites is similar, or even higher, and Li is clearly higher than in Panceiros pegmatites. Other incompatible elements, such as Zr and Y, have noticeably higher contents in granites than in pegmatites, whereas Hf, U, and W contents are quite similar. Barium is significantly higher in granites than in pegmatites, and Sr does not show a variation in concentration between granites on the one hand and pegmatites on the other.

Rare earth element (REE) concentrations from the studied pegmatites and granites are given in Table A9. REE contents are much lower in pegmatites than in granites. In fact, concentrations of some particular REEs (mostly Eu and HREEs) in the pegmatites are below the limit of detection (LOD) of the analytical technique. Presqueira pegmatite presents the lowest concentration in REEs, showing various rare earth elements below LOD (Table A9). The chondrite-normalized REE patterns [40] of these rocks are shown in the spider diagram of Figure 12. The three granite facies have low total REE concentrations (66.79–108.49 ppm) and uniform chondrite-normalized REE distribution patterns, with consistent La/Yb ratios and negative Eu anomalies, suggesting they are comagmatic. All granite facies are LREE-enriched (La/Sm of 4.48–4.74), with moderate HREE depletions (Gd/Yb of 5.32–5.40), and have distinct negative Eu anomalies (Eu/Eu* = 0.22–0.41). GRM granite shows the strongest LREE enrichment and negative europium anomaly. Pegmatites have complex, very variable chondrite-normalized REE patterns among sampled bodies. Considering the more complete REE patterns (i.e., larger number of REE contents above LOD), which are those of the Panceiros pegmatites, a common characteristic is that they are flatter than those of the granites. However, they show very variable LREE enrichment (La/Sm from 1.71 up to 6.87) and mostly flat HREE patterns (Gd/Yb from 0.64–1.90), the Eu anomaly being predominantly negative.

6.2. Pegmatite–Wallrock Interaction

In order to obtain information on the interaction between pegmatite-derived fluids and host-rock, representative samples from the schist adjacent to two pegmatitic bodies from Panceiros (Santa Baia schist) and to the Presqueira pegmatite (Paraño schist) were collected. In addition, samples of the corresponding host-schist were also collected, two samples from the Santa Baia group and two from the Paraño group. In order to collect these samples beyond the alteration halos of the pegmatites, the Paraño group samples were taken in the eastern limb of the Forcarei Synform, in areas where there are no pegmatite outcrops, and pegmatite occurrences are not documented in the literature. In the same way, samples from the Santa Baia group were taken at the southern end of the Cotobade Synform (Figure 2), where there are no pegmatite outcrops.

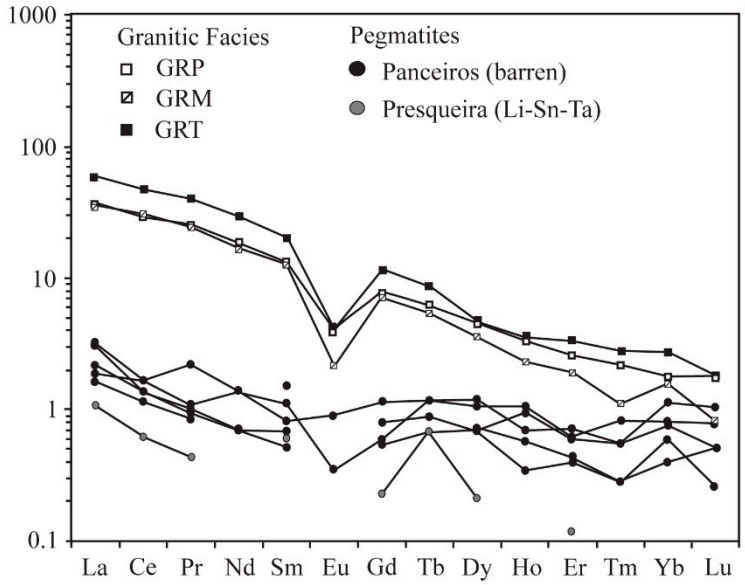

Figure 12. Chondrite-normalized rare earth element abundances [41] of representative whole-rock samples from the barren pegmatites of Panceiros and the Li–Sn–Ta mineralized pegmatite of Presqueira, and from the granite facies (GRP, GRM, and GRT) of the studied area. Note that REE contents are much higher in granites than in pegmatites, and the latter show incomplete patterns because some REEs are below the limits of detection of the analytical technique used.

The mineralogy of these samples was characterized by optical microscopy. The schist adjacent to the pegmatites shows a metasomatic mineralogical assemblage that overprints the metamorphic assemblage [42]. In both the Santa Baia and the Paraño schist, the dominant prograde metamorphic assemblage consists of quartz, biotite, muscovite, ±andalusite, ilmenite partially replaced by rutile and, in the Paraño schist, ± chlorite. The main metasomatic paragenesis of the schist at the contact of the Panceiros pegmatites is mainly made up of quartz, muscovite, biotite, and, in minor proportions, fluorapatite, oligoclase ($Ab_{85–87}$), and tourmaline. Some sulphides, pyrite, chalcopyrite, and galena occur as accessory minerals. The dominant metasomatic assemblage of the schist at the contact of the Presqueira pegmatite is similar. It mainly consists of quartz, muscovite, biotite, and, in less proportion, tourmaline, rutile, and Mn-bearing ilmenite (around 6 wt % MnO). Of special note is the presence of tiny (40–100 μm) crystals of a Zr-bearing phosphate, identified by SEM-EDS, adjacent to or as an overgrowth on rutile crystals [42]. Electron microprobe analyses (47.3 wt % P_2O_5, 29.9 wt % ZrO_2, 15.7 wt % FeO) allowed us to identify it as malhmoodite $FeZr(PO_4)_2$ $4H_2O$. A wider variety of sulphides occurs as accessory minerals: pyrite, chalcopyrite, galena, sphalerite, Ni–Co bearing löllingite, and arsenopyrite.

The whole-rock compositions of the sampled schists are shown in Table A10. To quantify the amounts of individual elements added to and subtracted from the wallrock schists overcoming the distortions of the closure effect, we have used the single precursor mass transfer technique [43]. The calculations have been performed for the major elements and, also, for the main trace elements that characterize the whole-rock compositions of the studied pegmatites. The first step, as in any mass transfer calculation, is to establish which elements act as immobile ones in the schist during the pegmatite–wallrock interaction. For this, we have plotted pairs of potentially immobile elements (i.e., Al, Ti, Zr, and Y) from the metasomatized schist of the pegmatite wallrock and the corresponding non-metasomatized schist on x–y bivariate diagrams with origins at zero. Several authors indicate that a highly correlated trend that passes through the origin with correlation coefficients exceeding 0.85 permits the selection of that pair of elements as immobile elements [44,45]. In the schist that hosts the Panceiros pegmatites, Ti vs. Zr gives an $R^2 = 0.99$. In the schist that hosts the Presqueira pegmatite, the highest correlation coefficients were that of Al vs. Y ($R^2 = 0.85$). Taking into account these values, we have done the mass transfer calculations for the metasomatized wallrock of Panceiros pegmatites

and of Presqueira pegmatite, using as immobile elements Ti and Al, respectively, in the following calculation [43]

$$\Delta^a = (Z^p/Z^a \times C^a) - C^p \quad (1)$$

where Δ^a is absolute mass change of element a; C^a concentration of component in metasomatized host-schist (wallrock); C^p concentration of component in non-metasomatized host-schist (precursor schist); Z^a concentration of immobile element in metasomatized host-schist (wallrock); Z^p concentration of an immobile element in non-metasomatized host-schist (precursor schist).

In addition, we have verified that similar results are obtained using the other possible immobile elements for the Panceiros pegmatite wallrock, i.e., Zr, and for the Presqueira pegmatite wallrock, i.e., Y. The results are shown in Table A11 and Figure 13.

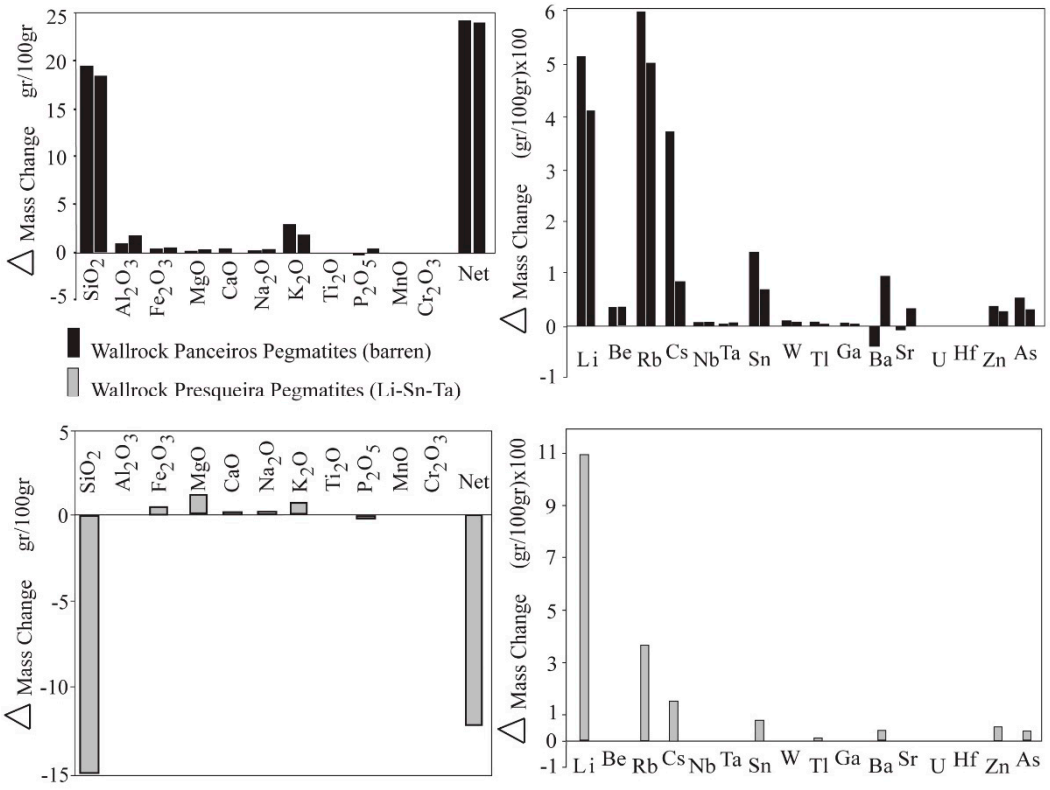

Figure 13. Bar diagrams showing estimated absolute mass changes (calculations according to [43]) of major and minor elements from the wallrock of two pegmatites from Panceiros (black bars) and from the wallrock of the Presqueira pegmatite (grey bars). The net mass change of major elements (Net) is also plotted.

From these data, we note that the wallrock schist of Panceiros pegmatites has a net mass gain mainly due to the addition of SiO_2 and, in minor proportions, Al_2O_3 and K_2O (Figure 13). This addition is consistent by the presence of neo-formed quartz, biotite, and muscovite in these alteration halos. However, the wallrock schist of the Presqueira pegmatite has a net mass loss, mainly due to the loss of SiO_2 (Figure 13). This silica loss could be associated with the strong ductile deformation affecting these rocks during D_3 shear that, as previously mentioned, developed mylonitic textures in the Presqueira pegmatite. Removal of large amounts of silica during shear zone formation has been reported by other authors [46,47]. Thus, this silica loss would not be related to the interaction between pegmatite-derived fluids and host-rock.

The most noteworthy results concern the trace-elements (Figure 13 and Table A11), the wallrock schists of both the Panceiros, and the Presqueira pegmatites showing a distinct gain in Li, Rb, Cs, Sn, Zn, and As despite the lack of Li- and/or Sn-bearing mineralization in Panceiros pegmatites. Similarly,

the wallrock of the latter shows a gain in beryllium and a slight gain in tantalum and niobium though Ta–Nb or Be-bearing minerals have not been recognized in the studied samples of the bodies. On the other hand, the wallrock schist of the Li–Sn–Ta mineralized body of Presqueira does not document a gain in Be or Ta–Nb. In both wallrock schists, there is an addition, in lower proportions, of W, Tl, and Ga. Several authors (e.g., [48] and reference therein) point out that late magmatic fluids export W more efficiently than Ta and Nb. Barium and strontium show variable behavior, being added or leached during the pegmatite–wallrock interaction. Other trace elements, such as uranium and hafnium, do not record a mass transfer high enough to be taken into account.

In order to check where these gained trace-elements were accommodated in the wallrock schist of the pegmatite bodies, EMP analyses were carried out on micas (biotite and muscovite) on samples from the non-metasomatized Paraño and Santa Baia schist, and samples from the metasomatized schists of the pegmatite wallrocks. The composition of the studied micas is plotted in the Monier and Robert [26] classification of Figure 14. Moreover, the neoformed oligoclase in the wallrock schists of the Panceiros pegmatites was also analyzed. As was shown in Table A12, the main trace elements in biotite are F, Cs, Rb, Ba, and Zn, whilst Cl, Ga, Sn, and Sr were below the detection limit. The data show an enrichment in Rb, Cs, and F in biotite from the wallrock schist of the Panceiros and Presqueira pegmatites, whereas the Ba content tends to be lower. The variations in the Zn contents are not important (Table A12). Figure 14 shows these variations in trace-element content in biotite from the non-metasomatized Santa Baia schist and from wallrock schist. In the latter case, the analyses are plotted in two separate fields, each corresponding to the wallrock of two different pegmatite bodies (samples ESQ-C and ESQ-4 in Table A12); the concentration of Li_2O in the biotite according to Tindle and Webb [49]. Taking this into account, the F-richer biotite from the wallrock may have had a higher Li contents (from 0.23 to 0.70 wt % Li_2O in the case of Panceiros pegmatites; from 0.24 to 0.54 wt % Li_2O in the case of Presqueira pegmatite) than that of the non-metasomatized schist (from 0.0 to 0.33 wt % Li_2O).

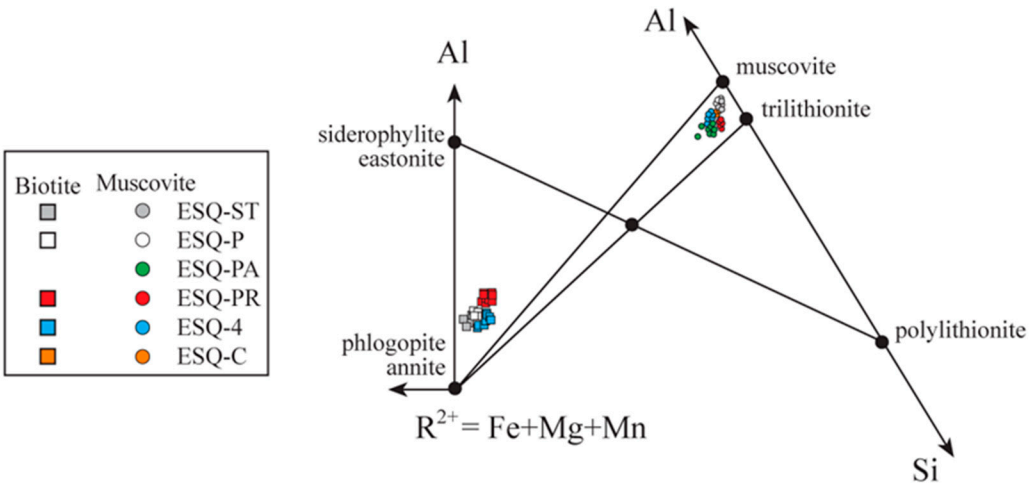

Figure 14. Chemical composition of micas from the pegmatite wallrocks and non-metasomatized schists plotted on the triangular diagram as a function of Al (IV + VI)–R^{2+}–Si (apfu), according to [26].

Microprobe analyses of muscovite from schist (Table A13) indicate that the main trace elements in this mineral are Rb and Ba, which were always detected, whereas Zn, Cs, and F were found in lower concentrations, sometimes below their respective LOD. In addition, Cl, Ga, Sn, and Sr were always below the LOD. As in the case of biotite, the muscovite from the metasomatized schist alongside Panceiros pegmatites are richer in Rb, Cs, and F and poorer in Ba than muscovite from the non-metasomatized Santa Baia Schist (Figure 15). The concentration of Li_2O in the muscovite was estimated using the empirical equation $0.3935 \times F^{1.326}$ [50], giving values of between 116 and 664 ppm for the F-richer muscovite from the wallrock. The electron-microprobe data for muscovite from the non-metasomatized schist of the Paraño Group and from the metasomatized wallrock schist of the

Presqueira pegmatite did not show differences in trace-element contents, which in the binary diagrams, are plotted together. For this reason, they are not included in Figure 15.

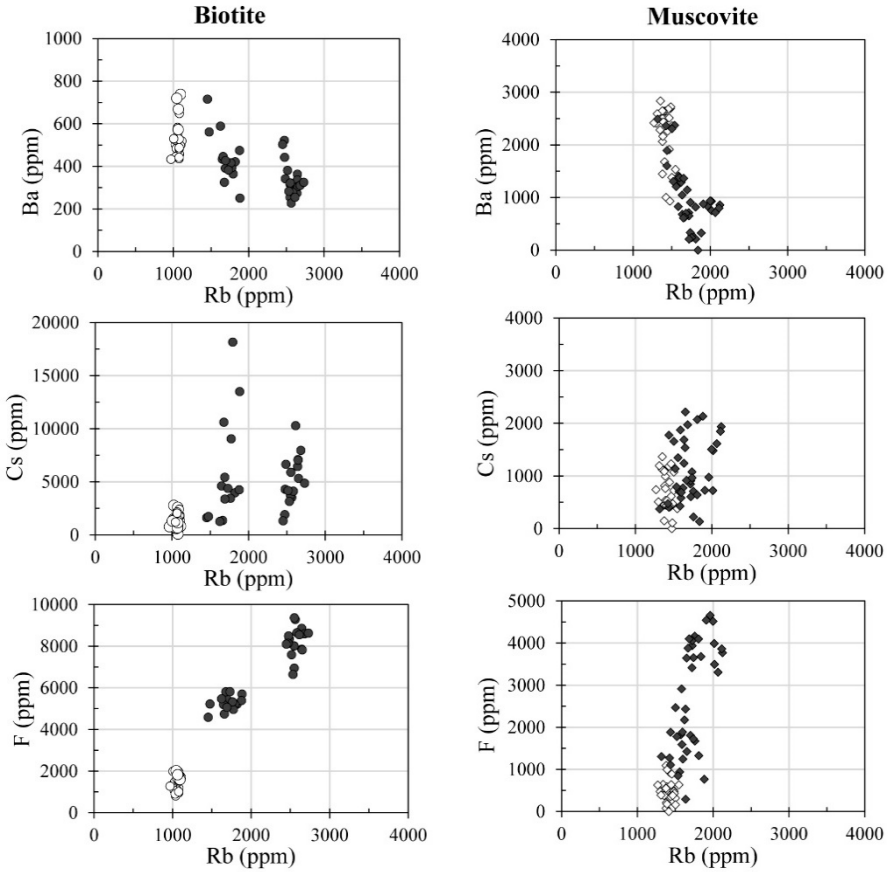

Figure 15. Trace-element diagrams (EPMA data) in biotite (circles) and muscovite (diamonds) from non-metasomatized Santa Baia schist (white) and metasomatized schist from the wallrock of the Panceiros pegmatites (black).

We also analyzed the trace elements in the oligoclase present in the metasomatized wallrock schist of the Panceiros pegmatites. The microprobe data showed that the main trace elements are Rb (around 2000 ppm Rb_2O), Sr (from 570 to 1200 ppm SrO), P (from 340 to 2570 ppm P_2O_5), and Zn (from 300 to 440 ppm ZnO). Only in one case was Cs found to be above the detection limit. The rest of the trace elements measured (Ba, F, Cl, Sn, Ga) were always below their detection limits.

In the walkrock of the Presqueira pegmatite, electronic microprobe analyses in the rutile and in the manganese-bearing ilmenite constantly detected niobium above the LOD, with concentrations between 320 ppm and 1800 ppm, the highest contents being in rutile. The associated Zr-bearing phosphate, malhmoodite, showed W contents constantly above the LOD (from 500 to 1169 ppm).

Taking into account the mineral geochemistry of the metasomatic assemblage from the wallrock schists and the mass transfer results of the host-schist lithogeochemistry, the prominent gain in Li, Rb, Cs, and Zn of the pegmatite wallrocks is supported by the trace-element content of, mainly, biotite, but also of muscovite. In the wallrock of the Presqueira pegmatite, the addition of As, and also Zn, is clearly correlated with by the presence of sulfides such as arsenopyrite, löllingite, and sphalerite. Arsenic is also added to the wallrock of Panceiros pegmatites. We consider that As occurs in some of the phases forming the sulfide assemblage of the wallrock (e.g., pyrite). As regards Sn, this is constantly and noticeably added during the metasomatism of the wallrock by the pegmatite-derived fluids. However, we have not found the Sn-bearing mineral phase. Rutile can accommodate a wide range of highly charged trace elements up to percent levels, e.g., Sn, Nb, Ta, or W, among others [51–53].

We have checked for the presence of these trace elements in rutile or in ilmenite, but only niobium was detected. We propose that Sn could be a trace-element in rutile or micas, but in concentrations below the limits of detection of the EMP attained in this study. Hence, micro-analytical techniques attaining lower limits of detection would be necessary to assert that these minerals are the carriers of the mentioned trace element.

7. Mineral Geochemistry: Fractionation Trends

Černý et al. [54] established, and several authors (e.g., [55–57]) corroborated, the utility of the K/Rb and K/Cs of K-feldspar and micas as guides for chemical fractionation among pegmatites and between pegmatites and associated granites. Figures 16 and 17 show K/Rb vs. Rb and K/Cs vs. Cs in K-feldspar and in muscovite, respectively, from the Panceiros bodies, from the Presqueira pegmatite, and from the granites outcropping in the area. The plot of K/Rb vs. Cs in K-feldspar is also shown in Figure 16. The K/Rb and K/Cs ratios decrease, and Rb and Cs concentrations increase, either in K-feldspar or in muscovite, from the granites to the Presqueira pegmatite, indicating a fractionation trend. Thus, the degree of magmatic differentiation is lower in Panceiros pegmatites than in the Presqueira pegmatite and is close to that of the granites. Finally, the plot of K/Rb vs. Cs in K-feldspar shows a trend from the granites to the studied pegmatites. This is consistent with a fractional crystallization in which the magmatic differentiation increases in this direction, Presqueira pegmatite having the higher degree of differentiation. This is also supported by the whole-rock compositions of the pegmatites and associated granites shown in Figure 11.

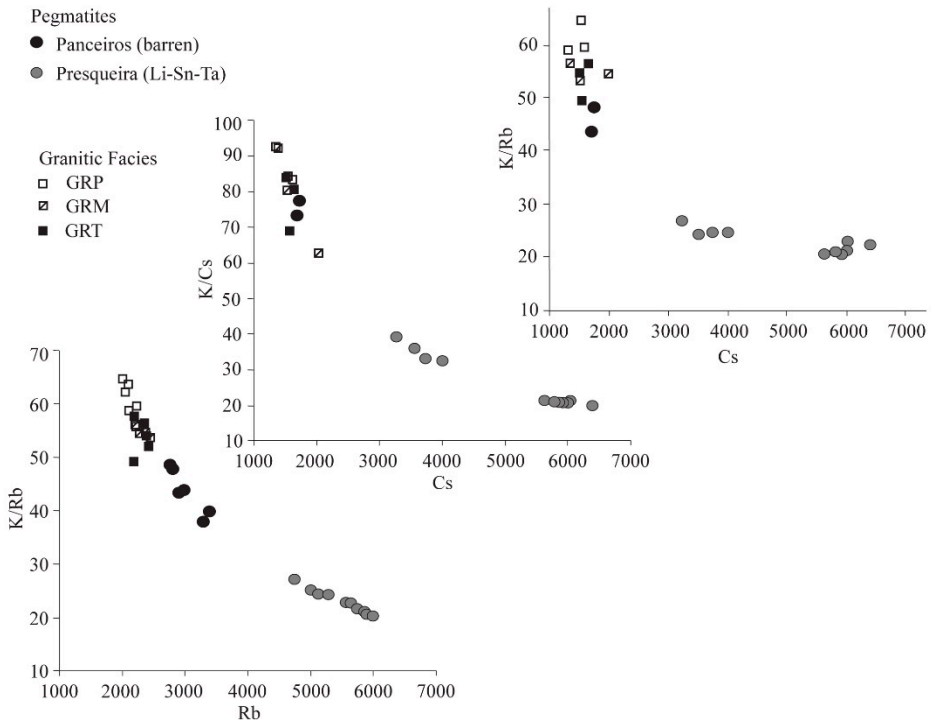

Figure 16. The K/Rb ratio vs. Rb and vs. Cs concentrations, and the K/Cs ratio vs. Cs concentration in K-feldspar from the barren pegmatites of Panceiros and the Li–Sn–Ta mineralized pegmatite of Presqueira, and from the granite facies (GRP, GRM, and GRT) of the studied area.

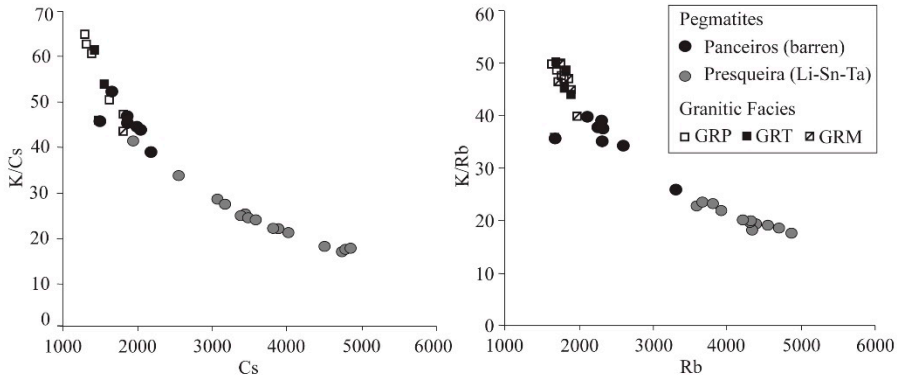

Figure 17. The K/Rb ratio vs. Rb content and the K/Cs ratio vs. Cs content in muscovite from the barren pegmatites of Panceiros and the Li–Sn–Ta mineralized pegmatite of Presqueira, and from the granite facies (GRP, GRM, and GRT) of the studied area.

8. Discussion and Conclusions

The mineralogical and geochemical studies of these selected pegmatites from Central Galicia point to a number of common and contrasting features between barren and Li–Sn–Ta mineralized pegmatites from this part of northwestern Iberia. These features are presented and discussed below.

As regards possible distinctive trace elements in major minerals, i.e., K-feldspar and muscovite, for use as a tool to prospect for Li–Sn–Ta mineralized pegmatites, our study shows that these minerals have the same type of trace elements in both barren and mineralized bodies, these trace elements being Rb, Cs, and P and, to a lesser degree, Zn and Ba. However, K-feldspar and muscovite of the Li–Sn–Ta mineralized body show the highest contents in Rb and Cs together with the lowest contents in P. It is noticeable that the muscovite with the highest F contents is in the barren bodies. Thus, high F contents may be characteristic of less evolved barren pegmatites genetically associated with Li–Sn–Ta mineralized bodies having spodumene as the main Li-bearing phase. Taking into account the empirical equations [50], the concentration of Li is proportional to the F contents in muscovite; muscovite with the highest F contents would, therefore, have the highest Li contents. Smeds [56] points out that in less fractionated pegmatites, i.e., Panceiros bodies in the current study, muscovite is probably the only Li-bearing mineral. This author also reports a strong correlation between elevated amounts of Sn in muscovite (>500 ppm), especially when coupled with low Mg and Fe, and the presence of cassiterite in Li–Sn bearing pegmatites in Sweden. Our study does not support this observation since with Mg and Fe being very low, the Sn contents obtained in the studied muscovite are always below the limit of detection (233 ppm).

Sn–Ta–(Nb) oxides have only been recognized in the Li–Sn–Ta mineralized Presqueira pegmatite, and two main trends of compositional evolution are shown by the Ta–Nb bearing oxides. The trend characterized by the increasing Ta ratio at near-constant Mn ratio indicates that the magmatic fractionation progressed from columbite-(Fe) to tantalite-(Fe) (Figure 8b,c,e and Figure 10). This fractionation trend is thought to be in accordance with low F activity [58–65]. The Presqueira pegmatite may represent an F-poor system, which it is also supported by the lack of lepidolite, as the Li-bearing phase, in this pegmatite. However, the presence of amblygonite may indicate conditions of not so low $mPFO_2$, leading to the stabilization of both Li-aluminosilicates and amblygonite-montebrasite [66]. The other trend, characterized by increasing the Ta ratio and decreasing Mn ratio (Figure 9a,b and Figure 10), is shown by crystals with oscillatory zonation of Nb-richer cores partially disrupted by patchy Ta-richer zonation, with anhedral tapiolite-(Fe) occurring at the margins of the grains or along microfractures. We consider that this tapiolite-(Fe) represents a later event superimposed on the earlier columbite–tantalite. We interpret this trend related to the replacement of early Nb-richer columbite–tantalite by a late generation richer in Ta. This is a common feature in rare-element granitic pegmatites (e.g., [38,48,64,65,67,68]). Some of these authors propose that

reactive fluids that separated from highly evolved residual albitic melts in the last stages of pegmatite crystallization are involved in these replacements. Since the albitization is a striking characteristic of the Li–Sn–Ta mineralized body in this study, a fluid separated from a Na-rich residual melt may have played an important role in the subsolidus evolution of this pegmatite. Hence, the re-equilibration of the earlier columbite–tantalite with this late fluid could have produced its partial resorption followed by the later crystallization of a Ta–Fe-richer oxide. This fluid could have also been the means of transport for the elements into the wallrock in a late magmatic subsolidus stage [69].

Both the barren and the Li–Sn–Ta mineralized pegmatites of this study have phosphates, though the paragenetic associations are different in each case. In the barren bodies, the textural relationships between phosphates and silicates support a metasomatic paragenesis of fluorapatite and eosphorite-childrenite replacing early silicates (Figure 3c,d). In the Li–Sn–Ta mineralized body, however, not all the phosphates are metasomatic in origin. In fact, the textural features allow us to establish that during the pegmatite evolution, P behaved compatibly during the final stages of the main silicate crystallization. Roda-Robles et al. [70] point out that P combines with Fe, Mn, and/or other elements to form primary Fe–Mn-rich and Al-rich phosphates. In the Li–Sn–Ta mineralized Presqueira pegmatite, these primary phosphates are fluorapatite and montebrasite. Later on, a new generation of fluorapatite and hydrated Al-bearing phosphate, goyazite, formed to replace early silicates, i.e., K-feldspar (Figure 7a,b). The mineralized body of Presqueira could be an open-system at the end of the crystallization, in a later subsolidus stage, allowing the penetration of elements, such as Sr, from host-rocks into the igneous body. A similar situation has been described in some Beauvoir granites [71]. Nevertheless, an internal origin due to the liberation of this element from the magmatic feldspars during their replacement/alteration cannot be discarded despite the measured Sr in feldspar being mainly below the LOD of the electronic microprobe (519 ppm). The above-mentioned fluid, which separated from a Na-rich residual melt, would also have been the means of transport for these elements. Finally, this body has veinlets filled with a paragenesis of hydrated phosphates (vivianite and messelite), together with sulfides such as sphalerite (Figure 7d). This paragenesis seems to represent an even later post-magmatic hydrothermal event.

A noticeable textural feature of the Li–Sn–Ta mineralized body is the previously described textures of the lithium aluminosilicates, the petalite replacement by both myrmekites and the spodumene + quartz intergrowth "SQI", and the quartz–spodumene symplectitic intergrowth at the contact with feldspars (Figure 6b,c). On the basis of these textures, we suggest a primary crystallization of petalite that was partially transformed into SQI during the cooling of the pegmatite, an evolution commonly observed by several authors (e.g., [57] and references therein). In addition, the residual albitic melt that caused the sodium metasomatism in the pegmatite also led to the partial transformation of petalite into albite + quartz (myrmekites) (Figure 6e,f) and the release of the lithium in the residual albitic melts. This favored spodumene crystallization during the albitization, and probably the development of quartz–spodumene symplectitic rims at the contact with the coeval albite. Other authors [72,73] also reported the coexistence of Li-aluminosilicates displaying interesting textures in some Li-rich aplite–pegmatites of northern Portugal. Hence, this is a stimulating point to encourage investigation of the pegmatites with Li-aluminosilicates in northwestern Iberia.

Whole-rock and mineral geochemistry of the studied pegmatites and the neighboring granites show fractionation trends that are consistent with magmatic differentiation increasing from the granites to the barren pegmatites and to the Li–Sn–Ta mineralized pegmatite. The latter attained the highest degree of magmatic differentiation (Figures 11, 16 and 17). The neighboring granites are peraluminous and strongly differentiated (Figure 11). The two-mica granite facies labeled GRM (Figure 2) would be the most evolved of them, a fact which is supported by the strongest europium anomaly of its REE pattern (Figure 12). As regards REE contents, there is REE depletion from the granite facies to the studied pegmatites. In fact, there is a remarkable disruption that disconnects the chondrite-normalized REE patterns and REE abundances of the neighboring granites from those of the studied pegmatites, even from the less-evolved barren pegmatites of Panceiros (Figure 12). A distinctive feature of the

Li–Sn–Ta mineralized Presqueira pegmatite is that it has the lowest concentrations in rare earth elements. The chondrite-normalized REE patterns of the studied pegmatites tend to be flat, variable, and complex, and the europium anomaly can be either negative or absent. These features agree with those described by several authors who compare the REE distribution patterns of pegmatites and their parental granites [74,75]. According to Černý [76], similar characteristics to those shown for the studied pegmatites are distinctive of granite-pegmatite sequences of the LCT family. This author proposes that these features are due to partial melting of metamorphic protoliths leaving REE-rich accessory minerals in the residua, to progressive REE-depletion of the differentiating melts by crystallization of some minerals (e.g., monazite, xenotime, apatite, garnet) and to a change in the oxidation state of europium. Complex variable chondrite-normalized REE patterns in pegmatites have been documented by several authors (e.g., [74–80]). As a possible explanation for the REE-patterns of the studied pegmatites, we suggest that late-magmatic to post-magmatic (hydrothermal) processes, and interaction with external metamorphic fluids, affected the studied bodies and probably remobilized some rare earth elements to produce the complex variable patterns. These stages involved the described replacement of primary silicates, such as K-feldspar or petalite by albite, and feldspars by phosphates.

From the current geochemical study of the pegmatite–wallrock interaction, the pegmatite-derived fluids that migrated into the surrounding host-rock were enriched in alkali metals such as Li, Rb, and Cs and, moreover, in Sn, Zn, and As (Figure 13). The presence of tourmaline in these alteration halos suggests that B also migrated to the country rock. According to London ([81] and references therein), tourmaline halos of pegmatite wallrocks are explained by mixing of two reservoirs: B-rich, hydrous peraluminous granitic melts (and vapor equilibrated with these melts) and typical host rocks (or fluids equilibrated with them) that contain sufficient Fe and Mg to exceed the solubility product of the tourmaline. This supports that the tourmalinization of host rocks adjacent to the studied pegmatites is due to the egress of B-rich aqueous fluids from pegmatites during the late stages of their consolidation. In addition to B, F also transferred from the pegmatite system into the host-schist since the metasomatic biotite of the wallrock is enriched in this halogen. Rubidium, Cs, F, and probably Li, enter the biotite more than the muscovite, as has been documented by other authors (e.g., [82]). London [57,83] points out that the formation of a biotite metasomatic aureole results in well-developed Li–Rb–Cs dispersion patterns around LCT pegmatites, and alkali metasomatism is a consequence of relatively high fluid–melt partition coefficients for Li, Rb, and Cs. Tin, Zn, and As also have relatively high fluid-melt partition coefficients, so they probably behaved in the same manner as did the alkali metals. Our results show that there is no difference in the suite of elements, i.e., B–F–Li–Rb–Cs–Sn–Zn–As, between the metasomatized wallrocks of the Panceiros pegmatites, less evolved and barren, and the Li–Sn–Ta mineralized body of Presqueira. In fact, only Li is clearly added in significant higher amounts to the wallrock of the ore-bearing Presqueira pegmatite. From the current results, the wallrock signature would not seem to be a useful tool for the exploration, at least for pegmatites from Central Galicia (northwestern Spain). However, London [83] states that wallrock alteration could provide clues for the exploration of internal zones. This author comments that "whereas the border zones of most pegmatites possess rather simple granite mineralogy and petrology, the chemistry of wallrock alteration reflects that of the innermost and most chemically fractionated portions of a pegmatite". Taking this into consideration, the possibility of the existence of more chemically fractionated zones carrying Li–Sn–Ta mineralization in the apparently barren bodies of Panceiros would be given, and, at the present level of erosion, these evolved zones would not outcrop.

Author Contributions: Conceptualization, A.R.L. and M.F.-F.; methodology, A.R.L. and M.F.-F.; validation, M.F.-F. and A.C.; formal analysis, A.R.L., M.F.-F. and A.C.; investigation, A.R.L., M.F.-F. and A.C.; writing—original draft preparation, A.R.L. and M.F.-F.; writing—review and editing, A.C. and A.M.-I.; visualization, A.R.L., M.F.-F. and A.C.; supervision, A.M.-I.; project administration, M.F.-F.; funding acquisition, M.F.-F., A.C. and A.M.-I.

Funding: This research was funded by Ministerio de Economía, Industria y Competitividad, Gobierno de España, project CGL2016-76532R (AEI/FEDER/UE).

Acknowledgments: The authors thank Solid Mines España, S.A.U for access to sample the Presqueira pegmatite and the data provided.

Conflicts of Interest: The authors declare no conflict of interest.

Appendix A

Table A1. Representative chemical compositions (major and trace elements) of K-feldspar from the barren pegmatites and the Li–Sn–Ta mineralized pegmatite.

	Barren Pegmatites (Panceiros)			**Li–Sn–Ta Mineralized Pegmatite (Presqueira)**			
wt % Oxide	**(a)**	**(b)**	**(c)**	**(a)**	**(b)**	**(c)**	**(d)**
SiO_2	64.38	63.71	63.62	63.47	64.38	63.17	63.68
Al_2O_3	18.88	19.38	18.94	18.55	18.65	18.30	18.29
Na_2O	0.48	1.03	1.52	0.90	0.41	0.59	0.99
K_2O	16.04	15.24	15.13	14.85	15.41	15.49	14.95
Rb_2O	0.37	0.36	0.32	0.64	0.62	0.52	0.63
Cs_2O	-	-	0.18	0.62	0.68	0.35	0.64
BaO	0.01	-	-	-	-	-	-
ZnO	0.02	0.02	0.01	0.02	0.02	-	0.01
P_2O_5	0.59	0.58	0.52	0.42	0.63	0.65	0.54
Total	100.77	100.32	100.24	99.47	100.8	99.07	99.73
Cations based on 8 Oxygens							
Si	2.96	2.93	2.94	2.96	2.97	2.96	2.97
Al	1.02	1.05	1.03	1.02	1.01	1.01	1.00
P	0.02	0.02	0.02	0.02	0.02	0.03	0.02
Sum Z	4.00	4.01	3.99	4.00	4.00	4.00	3.99
Na	0.04	0.09	0.14	0.08	0.04	0.05	0.09
K	0.94	0.89	0.89	0.88	0.91	0.93	0.89
Rb	0.01	0.01	0.01	0.02	0.02	0.02	0.02
Cs	-	-	-	0.01	0.01	0.01	0.01
Sum X	1.00	1.00	1.04	0.99	0.98	1.01	1.01
Trace elements (ppm)							
Rb	3384	3283	2893	5861	5645	4726	5738
P	2595	2524	2256	1842	2759	2831	2357
Cs	-	-	1704	5824	6424	3291	5999
Zn	146	139	91	134	141	-	112
Ba	124	-	-	-	-	-	-
K/Rb	39.36	38.52	43.40	21.03	22.66	27.21	21.63
K/Cs	-	-	73.69	21.16	19.91	39.07	20.69

Data from electronic microprobe analyses. -: below the limit of detection.

Table A2. Representative chemical compositions (major and trace elements) of plagioclase from the barren pegmatites and the Li–Sn–Ta mineralized pegmatite.

	Barren Pegmatites (Panceiros)				**Li–Sn–Ta Mineralized Pegmatite (Presqueira)**				
wt % Oxide	**(a)**	**(b)**	**(c)**	**(d)**	**(a)**	**(b)**	**(c)**	**(d)**	**(e)**
SiO_2	66.44	67.01	68.08	67.53	67.20	68.49	68.54	68.36	67.58
Al_2O_3	21.13	19.97	19.57	19.78	20.10	19.61	19.18	19.60	19.88
FeO	0.27	-	-	-	-	-	-	-	-
CaO	0.15	0.26	0.13	0.07	0.09	-	-	-	0.08
Na_2O	11.22	11.95	12.15	12.25	12.28	12.12	12.06	12.09	12.31
K_2O	0.17	0.15	0.15	0.10	0.07	0.07	0.12	0.09	0.09
Rb_2O	0.23	0.25	0.26	0.25	0.25	0.25	0.25	0.25	0.23
BaO	-	-	-	0.02	0.01	-	0.03	0.02	-
P_2O_5	0.80	0.54	0.13	0.50	0.65	0.04	0.15	0.08	0.56
Total	100.41	100.13	100.47	100.50	100.65	100.58	100.33	100.49	100.73
Cations based on 32 Oxygens									
Si	11.60	11.75	11.90	11.80	11.73	11.94	11.98	11.93	11.78
Al	4.35	4.13	4.03	4.08	4.13	4.03	3.95	4.03	4.08
P	0.12	0.08	0.02	0.07	0.10	0.01	0.02	0.01	0.08
Sum Z	16.06	15.96	15.95	15.95	15.96	15.98	15.95	15.97	15.94
Fe	0.04	0.00	0.00	0.00	0.00	0.00	0.00	0.00	0.00
Ca	0.03	0.05	0.02	0.01	0.02	0.00	0.00	0.00	0.01
Na	3.80	4.06	4.12	4.15	4.16	4.10	4.09	4.09	4.16
K	0.04	0.03	0.03	0.02	0.02	0.02	0.03	0.02	0.02
Rb	<0.01	<0.01	<0.01	<0.01	<0.01	<0.01	<0.01	<0.01	<0.01
Sum X	3.90	4.15	4.17	4.18	4.20	4.11	4.11	4.11	4.20
Ab	99.26	98.80	99.40	99.70	99.59	100.00	100.00	100.00	99.64
An	0.74	1.20	0.60	0.30	0.41	0.00	0.00	0.00	0.36
Trace elements (ppm)									
P	3502	2368	550	2181	2816	195	673	357	2458
Rb	2123	2242	2335	2274	2243	2274	2284	2245	2101
Ba	-	-	-	163	-	-	247	145	-

Data from electronic microprobe analyses. -: below the limit of detection.

Table A3. Representative chemical compositions (major and trace elements) of muscovite from the barren pegmatites and the Li–Sn–Ta mineralized pegmatite.

	Barren Pegmatites (Panceiros)					**Li–Sn–Ta Mineralized Pegmatite (Presqueira)**				
wt % Oxide	**(a)**	**(b)**	**(c)**	**(d)**	**(e)**	**(a)**	**(b)**	**(c)**	**(d)**	**(e)**
SiO_2	45.83	46.05	45.98	46.09	46.48	45.8	45.16	45.19	45.43	45.34
Al_2O_3	35.82	36.13	36.57	35.89	36.2	38.37	38.1	37.47	37.46	37.32
FeO	2.07	2.30	1.96	2.40	2.38	0.25	0.43	0.70	0.65	0.68
TiO_2	0.07	-	0.10	-	-	-	-	-	-	-
MgO	0.13	0.10	0.10	0.14	0.12	-	-	-	-	-
CaO	0.07	-	-	-	-	-	-	-	-	-
Na_2O	0.77	0.47	0.67	0.58	0.28	0.45	0.56	0.62	0.55	0.54
K_2O	9.92	10.12	10.21	10.3	10.09	10.56	9.78	10.21	10.24	10.26
Rb_2O	0.25	0.25	0.25	0.36	0.23	0.42	0.39	0.53	0.50	0.47
Cs_2O	-	0.23	0.18	0.20	-	0.33	0.21	0.41	0.51	0.37
BaO	-	-	-	-	-	-	0.01	0.01	0.02	0.02
P_2O_5	0.07	0.05	0.05	0.05	0.01	-	-	-	-	-
F	0.43	0.52	0.5	0.42	0.21	0.17	0.22	0.33	0.135	0.25
ZnO	0.04	0.04	0.03	0.04	0.05	0.02	0.04	0.04	0.05	0.04
LiO_2 *	0.13	0.16	0.16	0.12	0.05	0.04	0.05	0.09	0.03	0.06
H_2O *	4.27	4.27	4.30	4.33	4.43	4.52	4.40	4.33	4.44	4.37
O = F,Cl	0.19	0.22	0.21	0.18	0.09	0.07	0.09	0.14	0.05	0.10
Total	100.06	100.91	101.27	101.10	100.62	101.00	99.44	100.07	100.07	99.82
Cations based on 22 Oxygens										
Si	6.13	6.12	6.08	6.15	6.16	5.97	6.02	6.03	6.05	6.05
Al^{IV}	1.87	1.88	1.92	1.85	1.84	2.03	1.98	1.97	1.95	1.95
P	<0.01	<0.01	<0.01	<0.01	<0.01	-	-	-	-	-
Sum(Z)	8.00	8.00	8.00	8.00	8.00	8.00	8.000	8.00	8.00	8.00
Al^{VI}	3.77	3.77	3.78	3.75	3.81	4.01	4.00	3.93	3.94	3.93
Ti	<0.01	-	0.01	-	-	-	-	-	-	-
Fe	0.23	0.25	0.23	0.26	0.26	0.03	0.05	0.08	0.07	0.08
Mg	0.03	0.02	0.02	0.03	0.02	-	-	-	-	-
Zn	<0.01	<0.01	<0.01	<0.01	<0.01	<0.01	<0.01	<0.01	<0.01	<0.01
Li *	0.07	0.09	0.08	0.07	0.03	0.02	0.03	0.05	0.01	0.03
Sum (Y)	4.11	4.14	4.12	4.12	4.13	4.10	4.08	4.06	4.03	4.04
Ca	0.01	-	-	-	-	-	-	-	-	-
Na	0.20	0.12	0.17	0.15	0.07	0.11	0.15	0.16	0.14	0.14
K	1.69	1.75	1.76	1.74	1.70	1.76	1.66	1.74	1.74	1.75
Ba	-	-	-	-	-	-	<0.01	<0.01	<0.01	<0.01
Rb	0.02	0.02	0.02	0.03	0.02	0.03	0.03	0.05	0.04	0.04
Cs	-	0.01	0.01	0.01	-	0.02	0.01	0.02	0.03	0.02
Sum (X)	1.92	1.90	1.96	1.93	1.80	1.92	1.85	1.97	1.95	1.95
OH *	3.81	3.78	3.79	3.82	3.91	3.93	3.91	3.86	3.94	3.90
F	0.18	0.23	0.21	0.17	0.09	0.07	0.09	0.14	0.05	0.10
Trace elements (ppm)										
Rb	2321	2262	2312	3308	2133	3804	3602	4881	4572	4315
Cs	-	2204	1660	1884	-	3105	1963	3870	4829	3489
Zn	303	289	281	339	369	174	304	330	368	285
Ba	-	-	-	-	-	-	-	116	146	170
P	316	219	216	212	433	-	-	-	-	-
K/Rb	35.5	37.9	37.4	25.8	39.3	23.1	22.5	17.4	18.6	19.7

Data from electronic microprobe analyses. -: below the limit of detection; *: Li calculated according to $Li_2O = 0.3935F^{1.326}$ [50], H_2O calculated after Tindle and Webb [49].

Table A4. Representative chemical compositions of garnet from the barren pegmatites of Panceiros.

wt % Oxide	(a)	(b)	(c)	(d)	(e)	(f)	(g)	(h)	(i)	(j)	(k)
SiO_2	36.00	36.04	36.15	35.74	35.65	35.65	35.64	35.66	35.53	35.78	35.83
Al_2O_3	19.94	19.87	19.88	19.91	19.78	19.80	19.73	19.82	19.68	19.93	19.78
MgO	0.14	0.15	0.16	0.10	0.11	0.11	0.13	-	0.04	0.09	0.07
FeO	30.03	30.44	30.09	29.24	29.10	29.94	30.40	25.90	25.23	28.04	27.63
MnO	13.99	13.76	13.77	14.76	14.84	13.75	13.26	18.21	18.66	16.28	16.30
CaO	0.09	0.09	0.08	0.08	0.14	0.07	0.09	0.11	0.13	0.13	0.15
P_2O_5	0.21	0.34	0.29	0.36	0.26	0.31	0.23	0.28	0.34	0.30	0.29
Total	100.40	100.69	100.42	100.19	99.88	99.63	99.48	99.98	99.61	100.55	100.05
Cations based on 12 Oxygens											
Si	2.97	2.97	2.96	2.96	2.96	2.97	2.97	2.96	2.96	2.95	2.97
Al^{IV}	0.03	0.03	0.02	0.04	0.04	0.03	0.03	0.04	0.04	0.05	0.03
P	0.01	0.02	0.02	0.02	0.02	0.02	0.02	0.02	0.02	0.02	0.02
Al^{VI}	1.92	1.90	1.92	1.90	1.90	1.91	1.91	1.90	1.90	1.90	1.91
Fe^{3+}	0.06	0.07	0.06	0.06	0.07	0.06	0.06	0.07	0.07	0.07	0.07
Fe^{2+}	2.01	2.03	2.02	1.96	1.95	2.02	2.06	1.73	1.69	1.86	1.85
Mn	0.98	0.96	0.96	1.03	1.04	0.97	0.94	1.28	1.32	1.14	1.14
Mg	0.02	0.02	0.02	0.01	0.01	0.01	0.02	-	0.01	0.01	0.01
Ca	0.01	0.01	0.01	0.01	0.01	0.01	0.02	0.01	0.01	0.01	0.01
Total	8.01	8.01	8.00	8.01	8.01	8.01	8.01	8.01	8.01	8.01	8.01
Almandine	65.64	66.00	65.97	63.90	63.29	66.10	67.06	55.79	54.16	60.26	59.92
Espessartine	33.51	33.08	33.12	35.42	35.78	33.21	32.11	43.88	45.24	38.97	39.31
Andradite	0.27	0.29	0.24	0.25	0.44	0.20	0.26	0.34	0.40	0.40	0.46
Pyrope	0.58	0.63	0.68	0.44	0.48	0.49	0.56	0.00	0.19	0.37	0.31

Data from electronic microprobe analyses. -: below the limit of detection.

Table A5. Representative chemical compositions of phosphates from the barren pegmatites of Panceiros.

	Probable Hydroxylapatite	Mn-Rich Fluorapatite		Eosphorite–Childrenite			
wt % Oxide	(1)	(2)	(3)	(4)	(5)	(6)	(7)
P_2O_5	32.96	42.92	42.74	33.58	33.77	33.86	33.36
Al_2O_3	1.77	0.00	0.00	22.70	22.81	22.37	22.71
CaO	34.53	47.73	47.92	0.36	0.48	0.49	0.40
MnO	3.73	5.50	5.15	14.37	13.93	28.11	27.27
FeO	1.17	1.14	1.25	15.46	15.22	1.69	3.11
SrO	0.17	-	-	-	-	-	-
BaO	-	0.02	0.02	-	-	-	-
Rb_2O	0.05	-	-	-	-	-	-
K_2O	-	-	-	-	0.06	-	-
F	0.74	3.48	3.61	0.53	0.49	0.59	0.53
Cl	0.85	-	-	-	-	-	-
Total	75.97	100.79	100.68	87.01	86.75	87.10	87.37
O = F, Cl	0.50	1.47	1.52	0.22	0.21	0.25	0.22
Total	75.46	99.32	99.16	86.79	86.55	86.85	87.15
	Cations based on 5 PO_4			Cations based on 1 PO_4			
P	5.00	5.00	5.00	1.00	1.00	1.00	1.00
Al	0.37	-	-	0.94	0.94	0.92	0.95
Ca	6.63	7.04	7.10	0.01	0.02	0.02	0.01
Mn	0.57	0.64	0.60	0.43	0.41	0.83	0.82
Fe	0.18	0.13	0.14	0.45	0.44	0.05	0.09
Sr	0.018	-	-	-	-	-	-
K	-	-	-	-	0.06	-	-
Ba	-	<0.01	<0.01	-	-	-	-
Rb	<0.01	-	-	-	-	-	-
F	0.42	1.52	1.58	0.06	0.05	0.06	0.06
Cl	0.26	-	-	-	-	-	-
Fe/(Fe + Mn)	0.23	0.17	0.19	0.515	0.519	0.056	0.101

Data from electronic microprobe analyses. -: below the limit of detection.

Table A6. Representative chemical compositions of phosphates from the Li–Sn–Ta mineralized pegmatite of Presqueira.

	Fluorapatite	**Messelite**		**Goyazite**	**Vivianite**	**Montebrasite**	
wt % Oxide	**(1)**	**(2)**	**(3)**	**(4)**	**(5)**	**(6)**	**(7)**
P_2O_5	43.16	40.86	41.92	30.81	35.99	53.99	53.74
Al_2O_3	-	0.07	-	28.34	-	36.32	36.37
CaO	50.61	30.34	29.82	-	-	-	-
MgO	-	0.35	0.36	-	0.13	-	-
MnO	2.11	6.00	14.83	0.03	0.89	-	-
FeO	0.21	13.26	4.76	3.40	43.55	-	0.09
SrO	0.05	0.09	-	15.95	-	0.02	-
BaO	0.05	-	-	0.02	-	-	-
Rb_2O	0.01	-	0.01	0.02	-	-	-
ZnO	-	-	-	0.02	-	-	-
F	3.61	0.68	0.76	0.42	0.35	3.38	1.57
Cl	-	-	-	-	-	0.00	0.03
Total	99.80	91.65	92.45	79.00	80.91	93.71	91.79
O = F, Cl	1.52	0.29	0.32	0.18	0.15	1.42	0.67
Total	98.28	91.36	92.13	78.83	80.76	92.28	91.12
Based on	5 PO_4		2 PO_4			1 PO_4	
P	5.00	2.00	2.00	2.00	2.00	1.00	1.00
Al	-	<0.01	-	2.56	-	0.94	0.94
Ca	7.42	1.88	1.808	-	-	-	-
Mg	-	0.03	0.03	-	0.01	-	-
Mn	0.24	0.29	0.71	<0.01	0.05	-	-
Fe	0.02	0.64	0.22	0.22	2.39	-	<0.01
Sr	<0.01	<0.01	-	0.71	-	-	-
Ba	<0.01	-	-	<0.01	-	-	-
Rb	<0.01	-	-	<0.01	-	-	-
Zn	-	-	-	<0.01	-	-	
F	1.56	0.12	0.14	0.10	0.07	0.23	0.11
Cl	-	-	-	-	-	-	<0.01
Li *	-	-	-	-	-	1.000	1.000
Fe/(Fe + Mn)	-	0.69	0.24	0.99	0.98	-	-

Data from electronic microprobe analyses. -: below the limit of detection; *: Li calculated in motebrasite as Li = 1 − (Na + K).

Table A7. Representative chemical compositions of Sn–Ta–Nb oxides from the Li–Sn–Ta mineralized pegmatite of Presqueira.

	Columbite–Tantalite				**Tapiolite-(Fe)**	**Cassiterite**			
wt % Oxide	**(a)**	**(b)**	**(c)**	**(d)**	**(a)**	**(a)**	**(b)**	**(c)**	**(d)**
SnO_2	0.83	0.55	1.09	0.21	0.87	98.89	95.13	99.19	99.24
Ta_2O_5	19.52	27.19	45.59	58.17	77.54	0.87	3.40	1.28	0.59
Nb_2O_5	59.78	55.22	36.68	26.21	6.73	0.45	0.94	-	0.36
FeO	10.82	8.88	8.38	9.60	13.49	0.29	0.74	0.13	0.35
MnO	7.27	8.52	7.62	5.55	0.61	-	-	-	-
TiO_2	-	-	-	-	1.41	0.10	0.17	0.08	0.18
UO_2	1.25	-	-	-	-	-	-	-	-
ZnO	0.12	0.12	0.06	0.11	-	-	-	-	-
In_2O_3	-	-	-	-	-	0.13	0.15	0.14	0.16
Total	99.59	100.47	99.42	99.85	100.65	100.74	100.52	100.81	100.88
	Cations based on 6 Oxygens					Cations based on 2 Oxygens			
Fe	0.56	0.46	0.48	0.59	0.90	0.01	0.01	<0.01	0.01
Mn	0.38	0.45	0.45	0.34	0.04	-	-	-	-
Nb	1.67	1.56	1.14	0.87	0.24	<0.01	0.01	-	<0.01
Ta	0.33	0.46	0.86	1.15	1.69	0.01	0.02	0.01	<0.01
Sn	0.02	0.01	0.03	0.01	0.03	0.98	0.95	0.99	0.98
Ti	-	-	-	-	0.08	<0.01	<0.01	<0.01	<0.01
U	0.02	-	-	-	-	-	-	-	-
Zn	<0.01	0.01	<0.01	0.01	-	-	-	-	-
In	-	-	-	-	-	<0.01	<0.01	<0.01	<0.01
Mn/(Mn + Fe)	0.40	0.49	0.48	0.37	0.04				
Ta/(Ta + Nb)	0.16	0.23	0.43	0.57	0.87				

Data from electronic microprobe analyses. -: below the limit of detection.

Table A8. Representative whole-rock composition of the studied pegmatites and neighboring granites.

	Panceiros Pegmatites (Barren)					Presqueira Peg. (Li–Sn–Ta)	Two-Mica Granitic Facies		
Samples *	**PAN-1**	**PAN-2**	**PAN-3**	**PAN-4**	**PAN-5**	**PR**	**GRT**	**GRM**	**GRP**
wt % Oxide									
SiO_2	74.19	74.34	73.69	75.62	74.41	73.73	72.31	71.97	73.77
Al_2O_3	14.74	14.93	15.11	14.16	14.59	16.67	14.78	14.84	14.46
Fe_2O_3 **	0.71	0.83	0.71	0.84	0.79	0.43	2.01	1.63	1.43
MgO	0.01	0.06	0.02	0.04	0.07	0.01	0.36	0.26	0.26
CaO	0.43	0.17	0.17	0.17	0.12	0.2	0.58	0.41	0.67
Na_2O	4.92	4.38	4.24	3.97	4.17	4.95	3.13	3.03	3.26
K_2O	3.32	3.51	4.71	3.56	4.47	2.46	5.33	5.16	4.81
TiO_2	-	0.02	-	0.01	0.03	-	0.23	0.15	0.15
P_2O_5	0.68	0.33	0.44	0.36	0.24	0.52	0.28	0.35	0.23
MnO	0.09	0.08	0.13	0.08	0.02	0.03	0.04	0.03	0.02
Cr_2O_3	0.01	0.01	0.01	0.01	0.01	0.01	0.01	0.01	0.01
L.O.I.	0.8	1.3	0.7	1.1	1.0	0.8	0.8	2.1	0.8
Total	99.10	98.66	99.23	98.82	98.92	98.99	99.06	97.84	99.07
Na_2O/K_2O	1.48	1.25	0.90	1.12	0.93	2.01	0.59	0.59	0.68
ISA	1.26	1.36	1.25	1.36	1.25	1.54	1.35	1.40	1.37
A/CNK	1.18	1.32	1.22	1.32	1.22	1.49	1.23	1.31	1.23
A							55.15	69.22	52.51
B							39.98	28.74	26.23
Trace elements (ppm)									
Li	35	63	24	98	57	>2000	157	225	119
Be	95	40	5	54	1	145	2	8	5
Rb	469	325	468	439	382	999	384	404	250
Cs	14	13	11	23	17	59	18	23	17
Nb	20	22	17	28	15	66	15	16	9
Ta	4	7	4	16	4	64	2	3	1
Sn	30	27	24	38	27	845	11	23	12
W	5	7	5	5	5	3	6	6	5
Tl	3	2	3	3	2	7	2	2	1
Ba	10	26	7	7	9	3	256	161	187
Sr	51	16	9	10	6	95	58	39	50
U	18	7	8	10	4	12	12	14	7
Hf	1	1	1	1	1	2	3	2	2
Zr	15	16	14	11	15	21	101	70	69
Y	1	1	1	2	1	0.4	9	5	7
Zn	49	23	21	33	26	99	69	58	37
As	26	14	593	44	21	2	4	3	5

*: each label corresponds to an individual pegmatitic body, GRP (moderately leucocratic medium-grained two-mica granite), GRM (moderately leucocratic fine-grained two-mica granite), GRT (inhomogeneous granite); **: total iron expressed as Fe_2O_3; Na_2O/K_2O ratio is calculated from wt % oxide; ISA = Al_2O_3 − (Na_2O + K_2O), A/CNK = Al_2O_3 − (Na_2O + K_2O + CaO) in molar % oxide; A = Al − (K + Na + 2Ca), B = Fe + Mg + Ti (Debon and Lefort [40]); L.O.I. loss on ignition; -: below the limit of detection; >: above the upper limit of quantification.

Table A9. REE concentrations in whole-rock samples from the studied pegmatites and neighboring granites.

		Panceiros Pegmatites (Barren)					Presqueira Peg. (Li–Sn–Ta)	Two-Mica Granitic Facies		
REE (ppm)	***LOD*** **	**PAN-1**	**PAN-2**	**PAN-3**	**PAN-4**	**PAN-5**	**PR**	**GRT**	**GRM**	**GRP**
La	*0.1*	1.10	1.20	0.60	0.70	0.80	0.40	22.40	13.70	13.80
Ce	*0.1*	1.30	1.60	1.10	1.60	1.30	0.60	46.20	29.30	28.20
Pr	*0.02*	0.14	0.30	0.12	0.15	0.13	0.06	5.59	3.43	3.54
Nd	*0.3*	0.50	1.00	-	1.00	0.50	-	21.30	12.10	13.30
Sm	*0.05*	0.16	0.19	0.35	0.26	0.12	0.15	4.72	2.96	3.08
Eu	*0.02*	-	0.08	-	0.03	-	-	0.35	0.19	0.37
Gd	*0.05*	0.25	0.35	0.19	0.18	0.17	0.07	3.62	2.23	2.43
Tb	*0.01*	0.05	0.07	0.04	0.07	0.04	0.04	0.51	0.32	0.37
Dy	*0.05*	0.26	0.41	0.28	0.45	0.27	0.08	1.82	1.40	1.79
Ho	*0.02*	0.03	0.09	0.05	0.06	0.08	-	0.30	0.20	0.29

Table A9. *Cont.*

		Panceiros Pegmatites (Barren)					Presqueira Peg. (Li–Sn–Ta)	Two-Mica Granitic Facies		
REE (ppm)	***LOD*** **	**PAN-1**	**PAN-2**	**PAN-3**	**PAN-4**	**PAN-5**	**PR**	**GRT**	**GRM**	**GRP**
Er	*0.03*	0.10	0.16	0.11	0.18	0.15	0.03	0.83	0.48	0.66
Tm	*0.01*	0.01	0.03	0.01	0.02	0.02	-	0.10	0.04	0.08
Yb	*0.05*	0.15	0.20	0.10	0.28	0.19	-	0.68	0.41	0.45
Lu	*0.01*	0.01	0.03	0.02	0.04	0.02	-	0.07	0.03	0.07
∑ REE		4.06	5.71	2.97	5.02	3.79	1.43	108.49	66.79	68.43
Eu/Eu *		-	0.948	-	0.424	-	-	0.259	0.226	0.413
La/Yb		7.33	6.00	6.00	2.50	4.21	-	32.94	33.41	30.66
La/Sm		6.87	6.31	1.71	2.69	6.66		4.74	4.62	4.48
Gd/Yb		1.66	1.75	1.90	0.64	0.89		5.32	5.43	5.40

Each label corresponds to an individual pegmatitic body, GRP (moderately leucocratic medium-grained two-mica granite), GRM (moderately leucocratic fine-grained two-mica granite), GRT (inhomogeneous granite); *: $Eu = Eu\sqrt{Sm \times Gd}$; **: limit of detection (LOD) for each rare-earth element; -: below the limit of detection.

Table A10. Representative whole-rock compositions of host-schist of the studied pegmatites.

	Santa Baia Host-Schist of Panceiros Pegmatites (Barren)				Paraño Host-Schist of Presqueira Pegmatite (Li–Sn–Ta)		
	Schist		**Wallrock Schist**		**Schist**		**Wallrock Schist**
Samples	**ESQ-P**	**ESQ-STA**	**ESQ-C**	**ESQ-4**	**ESQ-PA**	**ESQ-S**	**ESQ-PR**
wt % Oxide							
SiO_2	58.01	56.37	62.36	61.42	62.73	58.84	53.27
Al_2O_3	21.24	22.95	18.78	19.42	18.99	20.97	23.21
Fe_2O_3 *	7.26	8.19	6.53	6.63	7.11	7.59	9.01
MgO	1.91	2.03	1.81	1.87	0.63	1.65	2.59
CaO	0.03	0.04	0.08	0.44	-	0.01	0.12
Na_2O	0.36	0.38	0.48	0.56	0.31	0.41	0.61
K_2O	4.41	4.67	6.04	5.29	4.14	4.84	6.12
TiO_2	0.91	0.87	0.74	0.74	0.82	0.75	0.92
P_2O_5	0.07	0.11	0.07	0.37	0.08	0.08	0.09
MnO	0.08	0.09	0.08	0.09	0.07	0.23	0.15
Cr_2O_3	0.016	0.017	0.014	0.015	0.014	0.014	0.017
L.O.I.	5.5	4.1	2.8	2.9	4.9	4.4	3.6
Total	99.78	99.82	99.76	99.77	99.8	99.78	99.72
Trace elements (ppm)							
Li	230.7	184.7	585.4	502.7	64.5	93.6	1365.3
Be	2	1	29	29	3	2	2
Rb	189.4	207	883.8	568.5	182.5	221.1	665.1
Cs	10.8	20.7	313	80.5	14.3	14.2	195.9
Nb	15.9	16.4	17.6	18	15	13.9	16.6
Ta	1.3	1.1	3.1	5	1.1	1.3	1.2
Sn	5	4	117	59	3	4	102
W	2.8	3.1	8.3	6.9	3.5	1.9	7.8
Tl	0.8	1.1	6.3	3.8	0.9	1.2	4.9
Ga	23.1	24.3	23.3	21.2	22.1	26.4	29.3
Ba	750	590	512	620	609	755	834
Sr	50.6	47.1	32.4	66.3	60.7	70.4	80.7
U	3.3	4.3	4.3	4.6	3.8	2.7	3.4
Hf	5.9	4.2	5.3	4.5	5.6	3.2	3.3
Zr	218.6	144.7	180.3	176.5	192.1	117.7	122.1
Y	22.6	33	19.6	21.3	21.7	26.2	27.1
Zn	85	102	106	97	44	108	148
As	5	7	48	29	-	8	52

Schist (non-metasomatized schist), Wallrock schist (metasomatized schist); *: total iron expressed as Fe_2O_3; L.O.I.: loss on ignition; -: below the limit of detection.

Table A11. Estimated absolute mass changes of major and minor elements from the metasomatized wallrocks of the studied pegmatites.

Pegmatite Locality	**Wallrock Schist of Pegmatites From Panceiros (Barren)**				**Presqueira (Li–Sn–Ta)**	
Samples	**ESQ-C**		**ESQ-4**		**ESQ-PR**	
Immobile Element Mass Change (gr/100gr)	**Ti**	***(Zr)*** *	**Ti**	***(Zr)****	**Al**	***(Y)*** *
Δ SiO_2	19.5	(*18.4*)	18.3	(*18.9*)	−14.9	(*−13.9*)
Δ Al_2O_3	1.0	(*0.7*)	1.8	(*2.0*)	0.0	(*0.5*)
Δ Fe_2O_3	0.3	(*0.2*)	0.4	(*0.5*)	0.4	(*0.6*)
Δ MgO	0.3	(*0.2*)	0.3	(*0.4*)	1.2	(*1.3*)
Δ CaO	0.1	(*0.1*)	0.5	(*0.5*)	0.1	(*0.1*)
Δ Na_2O	0.2	(*0.2*)	0.3	(*0.3*)	0.2	(*0.2*)
Δ K_2O	2.9	(*2.8*)	2.0	(*2.0*)	0.8	(*0.9*)
Δ TiO_2	0.0	(*0.0*)	0.0	(*0.0*)	0.0	(*0.0*)
Δ P_2O_5	0.0	(*0.0*)	0.4	(*0.4*)	0.0	(*0.0*)
Δ MnO	0.0	(*0.0*)	0.0	(*0.0*)	0.0	(*0.0*)
Δ Cr_2O_3	0.0	(*0.0*)	0.0	(*0.0*)	0.0	(*0.0*)
Net mass change	24.3	(*22.6*)	24.1	(*24.9*)	−12.3	(*−10.4*)
Mass change (gr/100gr) × 100						
Δ Li	5.12	(*5.02*)	4.10	(4.15)	10.97	(*11.24*)
Δ Be	0.34	(*0.34*)	0.34	(0.34)	−0.01	(*−0.01*)
Δ Rb	8.87	(*8.73*)	5.01	(5.06)	3.71	(*3.84*)
Δ Cs	3.69	(*3.64*)	0.83	(0.84)	1.54	(*1.58*)
Δ Nb	0.06	(*0.05*)	0.06	(0.06)	<−0.01	(*<0.01*)
Δ Ta	0.03	(*0.03*)	0.05	(0.05)	<−0.01	(*<−0.01*)
Δ Sn	1.39	(*1.37*)	0.68	(0.69)	0.84	(*0.86*)
Δ W	0.07	(*0.07*)	0.05	(0.06)	0.04	(*0.04*)
Δ Tl	0.07	(*0.07*)	0.04	(0.04)	0.03	(*0.03*)
Δ Ga	0.05	(*0.04*)	0.02	(0.03)	0.02	(*0.02*)
Δ Ba	−0.40	(*−0.49*)	0.92	(0.98)	0.39	(*0.56*)
Δ Sr	−0.09	(*−0.09*)	0.33	(0.33)	0.04	(*0.06*)
Δ U	0.01	(*0.01*)	0.02	(0.02)	<−0.01	(*<−0.01*)
Δ Hf	0.01	(*0.01*)	<0.01	(<0.01)	−0.01	(*−0.01*)
Δ Zn	0.37	(*0.35*)	0.26	(0.27)	0.58	(*0.61*)
Δ As	0.53	(*0.52*)	0.30	(0.30)	0.43	(*0.44*)

ESQ-C and ESQ-4: wallrock from two different pegmatites from Panceiros. ESQ-PR: wallrock from the Presqueira pegmatite; Δ: mass change calculated according to MacLean and Barrett [43]. See text for further explanation; Net mass change: ∑ Δ each major element; *: mass change calculated using the other possible immobile element (in brackets and italics).

Table A12. Representative chemical compositions of biotite from host-schist (non-metasomatized) and wallrock schist (metasomatized) of Panceiros and Presqueira pegmatites.

	Santa Baia Schist					**Panceiros Pegmatite Wallrock Schist**					**Presqueiras Pegmatite Wallrock Schist**		
	ESQ-ST			**ESQ-P**		**ESQ-C**		**ESQ-4**			**ESQ-PR**		
	5	**137**	**18**	**50**	**49**	**69**	**81**	**73**	**82**	**94**	**17**	**41**	**37**
SiO_2	34.23	33.49	34.17	34.26	34.05	34.94	34.59	35.18	35.42	35.18	34.79	35.02	34.87
TiO_2	2.70	2.57	2.39	2.13	2.06	2.04	2.48	2.10	2.25	1.75	1.37	1.36	1.36
Al_2O_3	19.31	19.31	19.37	19.07	19.29	18.73	18.41	18.23	18.94	18.42	19.49	20.04	20.17
FeO	21.98	24.51	22.49	22.74	22.50	22.57	22.96	23.49	21.79	22.42	22.63	21.79	21.96
MnO	0.26	0.25	0.21	0.18	0.24	0.33	0.30	0.47	0.35	0.34	0.40	0.32	0.34
MgO	6.86	6.31	6.80	6.95	7.01	6.78	6.45	6.64	6.62	6.42	6.71	7.13	6.85
CaO	0.03	-	0.03	-	-	0.03	-	-	0.04	-	-	-	-
Na_2O	0.34	0.21	0.31	0.23	0.27	0.10	0.21	0.15	0.27	0.24	0.12	0.18	0.19
K_2O	8.77	8.43	8.49	8.77	8.49	8.99	8.82	8.50	8.92	8.82	7.87	7.69	7.45
BaO	0.06	0.05	0.06	0.08	0.08	0.03	0.05	0.04	0.04	0.03	0.04	0.04	0.05
Rb_2O	0.12	0.11	0.11	0.12	0.12	0.21	0.20	0.27	0.28	0.29	0.21	0.20	0.20
Cs_2O	-	-	-	0.23	0.26	1.43	0.42	0.71	0.44	1.09	0.55	1.33	1.42
ZnO	0.08	0.05	0.08	0.05	0.05	0.10	0.10	0.08	0.07	0.06	0.05	0.04	0.05
F	0.17	0.13	0.20	0.20	0.16	0.57	0.52	0.84	0.76	0.86	0.47	0.48	0.40
Cl	-	-	-	-	-	-	-	-	-	-	-	-	-
Li_2O *	0.27	0.06	0.25	0.28	0.22	0.48	0.37	0.55	0.62	0.55	0.38	0.50	0.45
H_2O *	3.79	3.78	3.77	3.76	3.77	3.61	3.61	3.49	3.55	3.45	3.62	3.67	3.70
Subtotal	98.70	99.19	98.49	98.77	98.35	100.52	99.17	100.30	99.85	99.50	98.36	99.34	99.48
O = F,Cl	0.07	0.06	0.09	0.08	0.07	0.24	0.22	0.36	0.32	0.36	0.20	0.21	0.17
Total	98.63	99.14	98.41	98.69	98.28	100.28	98.95	99.95	99.52	99.14	98.16	99.13	99.31
Cations based on 22 Oxygens													
Si	5.30	5.23	5.30	5.33	5.31	5.39	5.38	5.43	5.43	5.47	5.39	5.39	5.38
Al^{IV}	2.70	2.77	2.70	2.67	2.69	2.61	2.62	2.57	2.57	2.53	2.61	2.61	2.62
Al^{VI}	0.82	0.78	0.85	0.82	0.86	0.80	0.76	0.74	0.85	0.84	0.98	1.02	1.05
Ti	0.31	0.30	0.28	0.25	0.24	0.24	0.29	0.24	0.26	0.20	0.16	0.16	0.16
Fe	2.85	3.20	2.92	2.96	2.93	2.91	2.99	3.03	2.79	2.91	2.95	2.80	2.83
Mn	0.03	0.03	0.03	0.02	0.03	0.04	0.04	0.06	0.04	0.04	0.05	0.04	0.04
Mg	1.58	1.47	1.57	1.61	1.63	1.56	1.50	1.53	1.51	1.49	1.56	1.64	1.57
Zn	0.01	0.01	0.01	0.01	0.01	0.01	0.01	0.01	0.01	0.01	0.01	0.00	0.01
Li *	0.17	0.04	0.16	0.18	0.14	0.30	0.23	0.34	0.38	0.34	0.24	0.31	0.28
Ca	0.00	0.00	0.01	0.00	0.00	0.00	0.00	0.00	0.01	0.00	0.00	0.00	0.00
Na	0.10	0.06	0.09	0.07	0.08	0.03	0.06	0.05	0.08	0.07	0.04	0.05	0.06
K	1.73	1.68	1.68	1.74	1.69	1.77	1.75	1.67	1.74	1.75	1.56	1.45	1.47
Ba	0.00	0.00	0.00	0.00	0.01	0.00	0.00	0.00	0.00	0.00	0.00	0.00	0.00
Rb	0.01	0.01	0.01	0.01	0.01	0.02	0.02	0.03	0.03	0.03	0.02	0.02	0.02
Cs	0.01	0.01	0.01	0.02	0.02	0.09	0.03	0.05	0.03	0.07	0.04	0.09	0.09
OH *	3.91	3.94	3.90	3.90	3.92	3.72	3.74	3.59	3.63	3.58	3.76	3.76	3.80
F	0.08	0.06	0.10	0.10	0.08	0.28	0.26	0.41	0.37	0.42	0.23	0.23	0.19

Data from electronic microprobe analyses. -: below the limit of detection; * Li_2O and H_2O calculated after Tindle and Webb [49].

Table A13. Representative chemical compositions of muscovite from host-schist (non-metasomatized) and wallrock schist (metasomatized) of Panceiros and Presqueira pegmatites.

	Santa Baia Schist			Panceiros Pegmatite Wallrock Schist			Paraño Group Schist		Presqueiras Pegmatite Wallrock Schist	
	ESQ-ST		ESQ-P	ESQ-C	ESQ-4		ESQ-PA		ESQ-PR	
	12	**141**	**32**	**87**	**86**	**91**	**106**	**115**	**6**	**26**
SiO_2	46.03	45.92	46.03	45.88	46.10	46.15	46.50	45.93	46.53	46.41
TiO_2	0.28	0.61	0.74	0.76	0.30	0.85	0.20	0.23	0.34	0.37
Al_2O_3	36.16	36.04	36.14	35.17	35.32	34.53	34.30	35.30	34.78	35.63
FeO	0.86	0.91	1.07	1.01	1.42	1.37	2.72	1.50	1.14	1.03
MnO	-	-	-	-	-	-	-	-	-	-
MgO	0.41	0.42	0.43	0.58	0.79	0.84	0.78	0.40	0.65	0.58
CaO	-	-	-	-	-	-	-	0.03	-	-
Na_2O	1.31	1.16	1.14	1.26	1.07	1.01	0.87	0.88	1.12	1.21
K_2O	9.70	9.54	9.83	9.57	10.14	9.86	9.76	8.84	9.27	9.48
BaO	0.28	0.28	0.30	0.26	0.08	0.08	0.15	0.16	0.22	0.21
Rb_2O	0.15	0.15	0.16	0.16	0.18	0.23	0.18	0.16	0.18	0.18
Cs_2O	-	0.02	-	0.18	0.21	0.17	0.07	0.11	-	-
ZnO	0.02	-	-	0.03		0.02	0.07	0.05	0.01	-
F	-	-	-	0.25	0.41	0.33	0.17	-	0.11	0.16
Cl	-	-	-	-	-	-	-	-	-	-
Li_2O *	-	-	-	0.06	0.12	0.09	0.04	-	0.02	0.04
H_2O *	4.48	4.48	4.50	4.37	4.31	4.33	4.41	4.41	4.42	4.43
Subtotal	99.66	99.52	100.36	99.53	100.44	99.86	100.21	97.99	98.81	99.72
O = F,Cl	0.03	0.02	0.02	0.10	0.17	0.14	0.07	0.03	0.05	0.07
Total	99.63	99.50	100.34	99.43	100.27	99.72	100.14	97.96	98.76	99.65
Cations based on 22 Oxygens										
Si	6.12	6.11	6.09	6.14	6.13	6.17	6.21	6.19	6.23	6.17
Al^{IV}	1.88	1.89	1.91	1.86	1.87	1.83	1.79	1.81	1.77	1.83
Al^{VI}	3.79	3.77	3.73	3.68	3.67	3.60	3.61	3.80	3.72	3.75
Ti	0.03	0.06	0.07	0.08	0.03	0.09	0.02	0.02	0.03	0.04
Fe	0.10	0.10	0.12	0.11	0.16	0.15	0.30	0.17	0.13	0.11
Mg	0.08	0.08	0.09	0.12	0.16	0.17	0.15	0.08	0.13	0.11
Zn	-	-	-	-	-	-	0.01	-	-	-
Li *	-	-	-	0.03	0.06	0.05	0.02	-	0.01	0.02
Na	0.34	0.30	0.29	0.33	0.28	0.26	0.22	0.23	0.29	0.31
K	1.65	1.62	1.66	1.63	1.72	1.68	1.66	1.52	1.58	1.61
Ba	0.01	0.01	0.02	0.01			0.01	0.01	0.01	0.01
Rb	0.01	0.01	0.01	0.01	0.02	0.02	0.02	0.01	0.02	0.02
Cs	0.01	0.01	0.00	0.01	0.01	0.01	0.00	0.01	0.01	0.00
OH *	3.97	3.98	3.98	3.89	3.83	3.86	3.93	3.97	3.95	3.93
F	0.03	0.02	0.02	0.10	0.17	0.14	0.07	0.03	0.05	0.07

Data from electronic microprobe analyses. -: below the limit of detection; *: Li calculated according to $Li_2O = 0.3935F1.326$ [50], H_2O calculated after Tindle and Webb [49].

References

1. Linnen, R.L.; Van Lichtervelde, M.; Černý, P. Granitic pegmatites as sources of strategic metals exploration and evaluation. *Elements* **2012**, *8*, 275–280. [CrossRef]
2. Fuertes-Fuente, M.; Martin-Izard, A. The Forcarei Sur rare-element granitic pegmatite field and associated mineralization, Galicia, Spain. *Can. Mineral.* **1998**, *36*, 303–325.
3. Fuertes-Fuente, M.; Martin-Izard, A.; Boiron, M.C.; Mangas, J. Fluid evolution of rare-element and muscovite granitic pegmatites from central Galicia, NW Spain. *Miner. Depos.* **2000**, *35*, 332–345. [CrossRef]
4. Canosa, F.; Martin-Izard, A.; Fuertes-Fuente, M. Evolved granitic systems as a source of rare element deposits: The Ponte Segade case (Galicia, NW Spain). *Lithos* **2012**, *153*, 165–176. [CrossRef]
5. Julivert, M.; Fontboté, J.M.; Ribeiro, A.; Nabais Conde, L.E. *Mapa Tectónico de la Península Ibérica y Baleares, E 1:1000000*; Memoria explicativa; Instituto Geológico y Minero de España: Madrid, Spain, 1972; 113p.

6. Farias, P.; Gallastegui, G.; González Lodeiro, F.; Marquínez, J.; Mantín Parra, L.M.; De Pablo Macía, J.G.; Rodríguez Fernández, L.R. Aportaciones al conocimiento de la litoestratigrafia y estructura de Galicia Central. *Mem. Fac. Ciências, Univ. Porto* **1987**, *1*, 411–431.
7. Farias, P.; Ordoñez-Casado, B.; Marcos, A.; Rubio-Ordoñez, A.; Fanning, C.M. U–Pb zircon SHRIMP evidence for Cambrian volcanism in the schistose domain within the Galicia-Trás-os-Montes zone (Variscan Orogen, NW Iberian Peninsula). *Geol. Acta* **2014**, *12*, 209–218.
8. Pérez-Estaún, A.; Bastida, F.; Martínez Catalán, J.R.; Gutiérrez Marco, J.C.; Marcos, A.; Pulgar, J.A. West Asturian–Leonese zone, stratigraphy. In *Pre-Mesozoic Geology of Iberia*; Dallmeyer, R.D., Martínez-García, E., Eds.; Springer: Berlin/Heidelberg, Germany, 1990; pp. 92–102.
9. Martínez-Catalán, J.R.; Arenas, R.; Díaz García, F.; Rubio Pascual, F.J.; Abati, J.; Marquínez, J. Variscan exhumation of a subducted Palaeozoic continental margin: The basal units of the Órdenes Complex, Galicia, NW Spain. *Tectonics* **1996**, *15*, 106–121. [CrossRef]
10. Díez Fernández, R.; Martínez Catalán, J.R.; Arenas, R.; Abati, J.; Gerdes, A.; Fernández-Suárez, J. U–Pb detrital zircon analysis of the lower allochthon of NW Iberia: Age constraints, provenance and links with the Variscan mobile belt and Gondwanan cratons. *J. Geol. Soc.* **2012**, *169*, 655–665. [CrossRef]
11. Ribeiro, A.; Pereira, E.; Dias, R. Central–Iberian zone. Allochthonous sequences. Structure in the geology of Iberia. In *Pre-Mesozoic Geology of Iberia*; Dallmeyer, R.D., Martínez-García, E., Eds.; Springer: Berlin/Heidelberg, Germany, 1990; pp. 237–246.
12. Martínez Catalán, J.R.; Arenas, R.; Díaz García, F.; Abati, J. Allochthonous units in the Variscan Belt of NW Iberia. In *Terranes and Accretionary History, Basement Tectonic*; Sinha, A.K., Ed.; Kluwer Academic Publishers: Dordrecht, The Netherlands, 1999; Volume 13, pp. 65–84.
13. Marcos, A.; Farias, P.; Galán, G.; Fernández, J.J.; Llana-Fúnez, S. Tectonic framework of the Cabo Ortegal Complex: A slab of lower crust exhumed in the Variscan orogeny (Northwestern Iberia Peninsula). In *Variscan-Appalachian Dynamics: The Building of the Late Paleozoic Basement*; Martínez Catalán, J.R., Hatcher, R.D., Arenas, R., Díaz García, F., Eds.; The Geological Society of America: Colorado, CO, USA, 2002; Volume 364, pp. 143–162.
14. Murphy, J.B.; Gutiérrez Alonso, G.; Fernández Suárez, J.; Braid, J.A. Probing crustal and mantle lithosphere origin through Ordovician volcanic rocks along the Iberian passive margin of Gondwana. *Tectonophysics* **2008**, *461*, 166–180. [CrossRef]
15. Barrera, J.L.; Farias, P.; González, F.; Marquínez, J.; Martín, L.M.; Martínez, J.R.; Del Olmo, A.; De Pablo, J.G. *Mapa Geológico 1: 200,000 de Ourense/Verín*; Memoria Explicativa; Publicación del Instituto Tecnológico Geominero de España: Madrid, Spain, 1989; 284p.
16. Marcos, A.; Llana-Fúnez, S. Estratigrafía y estructura de la lámina tectónica del Para-autóctono y de su autóctono en el área de Chantada (Galicia, NO de España). *Trab. de Geol.* **2002**, *23*, 53–72.
17. Farias, P.; Marcos, A. Dominio esquistoso de Galicia-tras-os-montes. In *Geología de España*; Vera, J.A., Ed.; SGE-IGME: Madrid, Spain, 2004; pp. 135–138.
18. Van Calsteren, P.W.C.; Boelrijk, N.A.I.M.; Hebeda, E.H.; Priem, H.N.A.; Den Tex, E.; Verdurmen, E.A.T.H.; Verschure, R.H. Isotopic dating of older elements (including the Cabo Ortegal mafic-ultramafic complex) in the Hercynian Orogen of NW Spain: Manifestations of a presumed Early-Paleozoic mantle-plume. *Chem. Geol.* **1979**, *24*, 35–36. [CrossRef]
19. Santos Zalduegui, J.F.; Schaérer, U.; Gil Ibarguchi, J.I. Isotope constraints on the age and origin of magmatism and metamorphism in the Malpica-Tuy allochton, Galicia, NW-Spain. *Chem. Geol.* **1995**, *121*, 91–103. [CrossRef]
20. Gil Ibarguchi, J.I.; Arenas, R. Metamorphic evolution of the allochthonous complexes from the northwest of Iberian Peninsula. In *Pre-Mesozoic Geology of Iberia*; Dallmeyer, R.D., Martínez-García, E., Eds.; Springer: Berlin/Heidelberg, Germany, 1990; pp. 237–246.
21. Arenas, R. Evolución Petrológica y Geoquímica de la Unidad Alóctona Inferior del Complejo Metamórfico Básico-Ultrabásico de Cabo Ortegal (Unidad de Moeche) y del Silúrico Parautóctono, Cadena Hercínica Ibérica (NW de España). Ph.D. Thesis, Universidad Complutense de Madrid, Madrid, Spain, 1985; 543p.
22. Ribeiro, A. Contribution a l'étude tectonique de Trás-Os-Montes Oriental. *Mem. Serv. Geol. Port.* **1974**, *24*, 1–168.

23. Dallmeyer, R.D.; Martínez Catalán, J.R.; Arenas, R.; Gil Ibarguchi, J.I.; Gutiérrez-Alonso, G.; Farias, P.; Aller, J.; Bastida, F. Diachronous Variscan tectonothermal activity in the NW Iberian Massif: Evidence from $^{40}Ar/^{39}Ar$ dating of regional fabrics. *Tectonophysics* **1997**, *277*, 307–337. [CrossRef]
24. Capdevila, R.; Vialette, Y. Estimation radiométrique de l'age de la deuxiéme phase tectonique hercynienne en Galice moyenne (Nord-Ouest de l'Espagne). *C. R. Acad. Sci.* **1970**, *270*, 2527–2530.
25. Plümber, O.; Putnis, A. The complex hydrothermal history of granitic rocks: Multiple feldspar replacement reactions under subsolidus conditions. *J. Petrol.* **2009**, *50*, 967–987. [CrossRef]
26. Monier, G.; Robert, J.L. Muscovite solid solutions in the system K_2O–MgO–FeO–$A1_2O_3$–SiO_2–H_2O: An experimental study at 2 kbar PH_2O and comparison with natural Li-free white micas. *Mineral. Mag.* **1986**, *50*, 257–266. [CrossRef]
27. Haggerty, S.E.; Fung, A.T.; Burt, D.M. Apatite, phosphorus and titanium in eclogitic garnet from the upper mantle. *Geophys. Res. Lett.* **1994**, *21*, 1699–1702. [CrossRef]
28. Burt, D.M. Compositional limits of phosphorus substitution in garnet in pegmatites and in the mantle. *Proc. Geol. Assoc. Can. Mineral. Assoc. Can.* **1996**, *2*, A-15.
29. Breiter, K.; Novák, M.; Koller, F.; Cempírek, J. Phosphorus—An omnipresent minor element in garnet of diverse textural types from leucocratic granitic rocks. *Mineral. Petrol.* **2005**, *85*, 205–221. [CrossRef]
30. Taylor, L.S.; Wise, M.A. Geochemistry and mode of occurrence of phosphorus in spessartine. In Proceedings of the Geological Society of America Annual Meeting, New Orleans, LA, USA, 6–9 November 1995; Volume 27, p. 470A.
31. Taylor, L.S.; Wise, M.A.; Simmons, W.B.; Falster, A.U. Occurrence of phosphorus in garnets from gem-bearing pegmatites. *Rock Miner.* **1997**, *3*, 189–190.
32. Anderson, S.D.; Cerný, P.; Halden, N.M.; Chapman, R.; Uher, P. The Yitt-B pegmatite swarm at Bernic Lake, southeastern Manitoba: A geochemical and paragenetic anomaly. *Can. Mineral.* **1998**, *36*, 283–301.
33. Pasero, M.; Kampf, A.R.; Ferraris, C.; Pekov, I.V.; Rakovan, J.; White, T.J. Nomenclature of the apatite supergroup minerals. *Eur. J. Mineral.* **2010**, *22*, 163–179. [CrossRef]
34. Bartlett, S.C. *Alberta-1 Rare Metals Project, Galicia, Spain, Mineral Resources, NI 43-101 Technical Report*; Solid Resources Limited: Vancouver, BC, Canada, 2014; 148p.
35. Černý, P.; Ferguson, R.B. The Tanco pegmatite at Bernic Lake, Manitoba; IV, Petalite and spodumene relations. *Can. Mineral.* **1972**, *11*, 660–678.
36. Hensen, B.J. Mineralogy and petrography of some tin-lithium and beryllium bearing albite pegmatites near Doade, Galicia (Orense). *Leidse Geol. Med.* **1967**, *39*, 249–259.
37. Feng, Y.; Liang, T.; Yang, X.; Zhang, Z.; Wang, Y. Chemical evolution of Nb–Ta oxides and cassiterite in phosphorus-rich albite–spodumene pegmatites in the Kangxiwa–Dahongliutan Pegmatite Field, Western Kunlun Orogen, China. *Minerals* **2019**, *9*, 166. [CrossRef]
38. Lahti, S.I. Zoning in columbite—Tantalite crystals from the granitic pegmatites of the Eräjärvi area, southern Finland. *Geochim. Cosmochim. Acta* **1987**, *51*, 509–517. [CrossRef]
39. Zhu, Z.Y.; Wang, R.C.; Marignac, C.; Cuney, M.; Mercadier, J.; Che, X.D.; Charles, N.; Lespinasse, M. Petrogenesis of Nb–(Ta) aplo-pegmatites and fine-grained granites from the Early Cretaceous Huangshan rare-metal granite suite, northeast Jiangxi Province, southeast China. *Lithos* **2019**, *346–347*, 105150. [CrossRef]
40. Debon, F.; Le Fort, P. A cationic classification of common plutonic rocks and associations: Principles, method, application. *Bull. Minéral.* **1988**, *111*, 493–510. [CrossRef]
41. Taylor, S.R.; Mclennan, S.H. *The Continental Crust: Its Composition and Evolution*; Blackwell: Oxford, UK, 1985; 312p.
42. Fuertes-Fuente, M.; Cepedal, A.; Martin-Izard, A. Mineralogical study of the wallrock metasomatism in barren and Li–Sn–Ta mineralized pegmatites from NW Spain (Central Galicia). *Can. Mineral.* **2019**, *57*, 741–743. [CrossRef]
43. Maclean, W.H.; Barrett, T.J. Lithogeochemical techniques using immobile elements. *J. Geochem. Explor.* **1993**, *48*, 109–133. [CrossRef]
44. Finlow-Bates, T.; Stumpfl, E.F. The behaviour of the so-called immobile elements in hydrothermally altered rocks associated with volcanogenic submarine exhalative ore deposits. *Miner. Deposita* **1981**, *16*, 319–328. [CrossRef]

45. Barret, T.J.; Mclean, W.H. Chemostratigraphy and hydrothermal alteration in exploration for VHMS deposits in greenstones and younger volcanic rocks. In *Alteration and Alteration Processes Associated with Ore Forming Systems*; Lentz, D.R., Ed.; Geological Association of Canada: St. John's, NL, Canada, 1994; Volume 11, pp. 433–467.
46. O'Hara, K. Fluid flow and Volume loss during mylonitization: An origin for phyllonite in an overthrust setting, North Carolina, USA. *Tectonophysics* **1988**, *156*, 21–36. [CrossRef]
47. Selverstone, J.; Morteani, G.; Staude, J.M. Fluid channelling during ductile shearing: Transformation of granodiorite into aluminous schist in the Tauern Window, Eastern Alps. *J. Metamorph. Geol.* **1991**, *9*, 419–431. [CrossRef]
48. Zhu, Z.Y.; Wang, R.C.; Che, X.D.; Zhu, J.C.; Wei, X.L.; Huang, X.E. Magmatic–Hydrothermal rare-element mineralization in the Songshugang granite (northeastern Jiangxi, China): Insights from an electron-microprobe study of Nb–Ta–Zr minerals. *Ore Geol. Rev.* **2015**, *65*, 749–760. [CrossRef]
49. Tindle, A.G.; Webb, P.C. Estimation of lithium contents in trioctahedral micas using microprobe data: Application to micas from granitic rocks. *Eur. J. Mineral.* **1990**, *2*, 595–610. [CrossRef]
50. Tischendorf, G.; Gottesmann, B.; Förster, H.J.; Trumbull, R.B. On Li-bearing micas: Estimating Li from electron microprobe analysis and an improved diagram for graphical representation. *Mineral. Mag.* **1997**, *61*, 809–834. [CrossRef]
51. Deer, W.A.; Howie, R.A.; Zussmann, J. *An Introduction to Rock-Forming Minerals*; Longman Scientific and Technical: New York, NY, USA, 1992; 696p.
52. Zack, T.; Kronz, A.; Foley, S.F.; Rivers, T. Trace element abundances in rutile from eclogites and associated garnet mica schists. *Chem. Geol.* **2002**, *184*, 97–122. [CrossRef]
53. Müller, A.; Halls, C. Rutile-the tin-tungsten host in the intrusive tourmaline breccia at Wheal Remfry, SW England. In *Mineral Deposit Research: Meeting the Global Challenge*; Mao, J., Bierlein, P.F., Eds.; Springer: Berlin/Heidelberg, Germany, 2005; pp. 441–444.
54. Černý, P.; Trueman, D.L.; Ziehlke, D.V.; Goad, B.E.; Paul, B.J. *The Cat Lake-Winnipeg River and the Wekusko Lake Pegmatite Fields*; Manitoba Department of Energy and Mines, Mineral Resources Division: Manitoba, ON, Canada, 1981; 216p.
55. Trueman, D.L.; Černý, P. Exploration for rare-element granitic pegmatites. In *Granitic Pegmatites in Science and Industry*; Černý, P., Ed.; Mineralogical Association of Canada: Québec, QC, Canada, 1982; Volume 8, pp. 463–494.
56. Smeds, S.A. Trace elements in potassium-feldspar and muscovite as a guide in the prospecting for lithium- and tin-bearing pegmatites in Sweden. *J. Geochem. Explor.* **1992**, *42*, 351–369. [CrossRef]
57. London, D. *Pegmatites*; The Canadian Mineralogist, Special Publication: Québec, QC, Canada, 2008; Volume 10, 340p.
58. Černý, P.; Ercit, S. Some recent advances in the mineralogy and geochemistry of Nb and Ta in rare-element granitic pegmatites. *Bull. Mineral.* **1985**, *108*, 499–532. [CrossRef]
59. Černý, P.; Ercit, S. Mineralogy of niobium and tantalum: Crystal chemical relationships, paragenetic aspects and their economic implications. In *Lanthanides, Tantalum and Niobium*; Möller, P., Černý, P., Saupé, F., Eds.; Springer: New York, NY, USA, 1989; pp. 27–29.
60. Wise, M.A.; Meintzer, R.E.; Černý, P. The Yellowknife pegmatite field: Mineralogy and geochemistry of Nb-Ta-Sn oxide minerals. In *Contribution to the Geology of the Northwest Territories*; Geology Division, INAC: Yellowknife, NT, Canada, 1986; Volume 2, pp. 15–25.
61. Černý, P. Geochemical and petrogenetic features of mineralization in rare-element granitic pegmatites in the light of current research. *Appl. Geochem.* **1992**, *7*, 393–416.
62. Spilde, M.N.; Shearer, C.K. A comparison of tantalum-niobium oxide assemblages in two mineralogically distinct rare-element granitic pegmatites, Black Hills, South Dakota. *Can. Mineral.* **1992**, *30*, 719–737.
63. Uher, P.; Černý, P.; Novák, M.; Siman, P. Niobium–tantalum minerals from granitic pegmatites in the Malé Karpaty, Považský Inovec and Žiar Mountains, Western Carpathians, Slovakia. *Miner. Slovaca* **1994**, *26*, 157–164.
64. Abella, P.A.; Corbella, M.; Melgarejo, J.C. Nb–Ta- minerals from the Cap de Creus pegmatite field, eastern Pyrenees: Distribution and geochemical trends. *Mineral. Petrol.* **1995**, *55*, 53–69. [CrossRef]
65. Tindle, A.G.; Breaks, F.W. Columbite–tantalite mineral chemistry from rare-element granitic pegmatites: Separation Lake area, N.W. Ontario, Canada. *Mineral. Petrol.* **2000**, *70*, 165–198. [CrossRef]

66. London, D. Stability of spodumene in acidic and saline fluorine-rich environments. *Carnegie Inst. Geophys. Lab. Annu. Rep.* **1982**, *81*, 331–334.
67. Canosa, F.; Fuertes-Fuente, M.; Martín-Izard, A. Mineralization of Sn–Ta–Nb oxides in Ponte Segade Deposit (North of Galicia, NW Spain). In *Let's Talk Ore Deposits*; Barra, F., Reich, M., Campos, E., Tornos, F., Eds.; Ediciones Universidad Católica del Norte: Antofagasta, Chile, 2011; pp. 163–165.
68. Chudík, P.; Uher, P.; Gadas, P.; Škoda, R.; Pršek, J. Niobium-tantalum oxide minerals in the Jezuitské Lesy granitic pegmatite, Bratislava Massif, Slovakia: Ta to Nb and Fe to Mn evolutionary trends in a narrow Be, Cs-rich and Li, B-poor dike. *Mineral. Petrol.* **2011**, *102*, 15–27. [CrossRef]
69. Wood, S.A.; Williams-Jones, A.E. Theoretical studies of the alteration of spodumene, petalite, eucryptite and pollucite in granitic pegmatites: Exchange reactions with alkali feldspars. *Contrib. Mineral. Petrol.* **1993**, *114*, 255–263. [CrossRef]
70. Roda-Robles, E.; Vieira, R.; Pesquera, A.; Lima, A. Chemical variations and significance of phosphates from the Fregeneda-Almendra pegmatite field, Central Iberian Zone (Spain and Portugal). *Mineral. Petrol.* **2010**, *100*, 23–34. [CrossRef]
71. Charoy, B.; Chaussidon, M.; Le Carlier De Veslud, C.; Duthou, J.L. Evidence of Sr mobility in and around the albite-lepidolite-topaz granite of Beauvoir (France): An in-situ ion and electron probe study of secondary Sr-rich phosphates. *Contrib. Mineral. Petrol.* **2003**, *145*, 673–690. [CrossRef]
72. Charoy, B.; Noronha, F.; Lima, A. Spodumene–petalite–eucryptite: Mutual relationships and pattern of alteration in li-rich aplite–pegmatite dykes from northern Portugal. *Can. Mineral.* **2001**, *39*, 729–746. [CrossRef]
73. Dias, F.; Lima, A.; Roda-Robles, E. Mutual relationships between spodumene and petalite from the Iberian Massif pegmatites: More than PT changes? *Can. Mineral.* **2019**, *57*, 731–732. [CrossRef]
74. Černý, P. Petrogenesis of granitic pegmatites. In *Granitic Pegmatites in Science and Industry*; Černý, P., Ed.; Mineralogical Association of Canada: Québec, QC, Canada, 1982; Volume 8, pp. 405–461.
75. Simmons, W.B.; Lee, M.T.; Brewster, R.H. Geochemistry and evolution of the South Platte granite–pegmatite system, Jefferson County, Colorado. *Geochim. Cosmochim. Acta* **1987**, *51*, 455–471. [CrossRef]
76. Černý, P. REE trends in rare-element granitic pegmatites: Enrichment vs. depletion in granite-to-pegmatite sequences. *J. Geosci.* **1997**, *42*, 34.
77. Wu, F.; Sun, D.Y.; Jahn, B.M.; Wilde, S. A Jurassic garnet-bearing granitic pluton from NE China showing tetrad REE patterns. *J. Asian Earth Sci.* **2004**, *23*, 731–744. [CrossRef]
78. Černý, P.; Masau, M.; Goad, B.E.; Ferreira, K. The Greer Lake leucogranite Manitoba and the origin of lepidolite-subtype granitic pegmatites. *Lithos* **2005**, *80*, 305–321. [CrossRef]
79. Lee, S.G.; Shin, S.C.; Jin, M.S.; Ogasawara, M.; Yang, M.K. Two Paleoproterozoic strongly peraluminous granitic plutons (Nonggeori and Naedeokri granites) at the northeastern part of Yeongnam Massif, Korea: Geochemical and isotopic constraints in East Asian crustal formation history. *Precambrian Res.* **2005**, *139*, 101–120. [CrossRef]
80. Beurlen, H.; Rhede, D.; Da Silva, M.R.R.; Thomas, R.; Guimarães, I.P. Petrography, geochemistry and chemical electron microprobe U–Pb–Th dating of pegmatitic granites in Borborema Province, North-eastern Brazil: A possible source of the rare-element granitic pegmatites. *Terrae* **2008**, *3*, 65–74.
81. London, D. Experimental synthesis and stability of tourmaline: A historical overview. *Can. Mineral.* **2011**, *49*, 117–136. [CrossRef]
82. Shearer, C.K.; Papike, J.J.; Simon, S.B.; Laul, J.C. Pegmatite–wallrock interactions, Black Hills, South Dakota: Interaction between pegmatite-derived fluids and quartz-mica schist wallrock. *Am. Mineral.* **1986**, *71*, 518–539.
83. London, D. Geochemistry of alkali and alkaline earth elements in ore-forming granites, pegmatites and rhyolites. In *Rare Element Geochemistry and Mineral Deposits*; Linnen, R.L., Samson, I.M., Eds.; Geological Association of Canada: St. John's, NL, Canada, 2005; Volume 17, pp. 17–43.